Turbulent flow separation around a ROV body

Koffi Danoh

Master Thesis

presented in partial fulfillment
of the requirements for the double degree:
“Advanced Master in Naval Architecture” conferred by University of Liege
"Master of Sciences in Applied Mechanics, specialization in Hydrodynamics,
Energetics and Propulsion” conferred by Ecole Centrale de Nantes

developed at "Dunarea de Jos" University of Galati
in the framework of the

“EMSHIP”
Erasmus Mundus Master Course
in “Integrated Advanced Ship Design”

Ref. 159652-1-2009-1-BE-ERA MUNDUS-EMMC

Supervisor: Prof. Costel Ungureanu, "Dunarea de Jos" University of Galati

Reviewer: Prof. Nikolai Kornev, University of Rostock

Galati, February 2014

CONTENTS

Declaration of Authorship

I Koffi Danoh Kouassi Ange Gatien declare that this thesis and the work presented in it are my own and have been generated by me as the result of my own original research.
"Turbulent flow separation around a ROV body"
Where I have consulted the published work of others, this is always clearly attributed.

Where I have quoted from the work of others, the source is always given. With the exception of such quotations, this thesis is entirely my own work.

I have acknowledged all main sources of help.

Where the thesis is based on work done by myself jointly with others, I have made clear exactly what was done by others and what I have contributed myself.

This thesis contains no material that has been submitted previously, in whole or in part, for the award of any other academic degree or diploma.

I cede copyright of the thesis in favour of the University of Galati

Date: 20.01.2014 *Signature* 

ABSTRACT

This report is the result of the master's thesis developed at the University of Galati in the frame of the EMSHIP Erasmus Mundus Master Course. It deals with the numerical simulation of the turbulent flow around a fully submerged Remotely Operated Vehicle (ROV) with ellipsoidal body using the commercial CFD code FLUENT. This ROV has as propulsion system four ducted propellers, two for horizontal displacement and two for vertical displacement.

The purpose of this study was to investigate the propulsive performance of this underwater vehicle by computational fluid dynamics method.

Two types of 3D geometry of this ROV have been created using the CAD software Rhinoceros 3D.

- The ellipsoidal ROV without propellers called bare body;
- And the ellipsoidal ROV with channels and propellers as defined in the scope of work. It is called ROV body.

Propellers are modeled as active disk and mounted in two cylindrical channels parallel with x-axis and the other two in channels parallel with z-axis.

FLUENT code was employed to compute the incompressible RANS equations on structured and unstructured mesh by using a finite volume technique in order to access the forces acting on the ROV and the flow field structure.

In order to choose the best turbulence model suited for the viscous incompressible flow around ROV body available in Fluent, we apply a Verification and Validation method.

In order to investigate the numerical error we have defined 3 types of mesh on the bare body, fine, medium and coarse. With each type of mesh we have run computations with all models of turbulence. After that we will compare with the towing tank results, in order to compute the modeling uncertainty.

The simulations are performed at Reynolds number $Re = 7.68 * 10\text{^}5$, which correspond to the service speed of 3 knots in freshwater conditions according to FLUENT.

The numerical simulations were performed on the ROV at five speeds of interest ranging from 1 m/s to 2 m/s. Propellers were substituted by an active disk for which the pressure jump is defined as boundary conditions.

Conclusions and recommendations are presented, as well as suggestions about future work related to the topic.

LIST OF FIGURES

LIST OF TABLES

ACRONYMS

ROV: Remotely Operated Vehicle (Underwater)

CFD: Computational Fluid Dynamics

CAD: Computer-Aided Design

EFD: Experimental Fluid Dynamics

PISO: Pressure Implicit with Splitting of operators

SIMPLE: Semi-Implicit Method for Pressure Linked Equations

NOMENCLATURE

A_0 Cross-sectional area of the disk

B Width of the ROV

C_D Drag coefficient

C_M Moment coefficient

C_p Pressure coefficient

C_L Lift coefficient

d Propeller diameter

ϵ Dissipation rate

H Height of the ROV

I Depth rating

k Turbulent kinematic energy

L Length of the ROV

Δp Pressure difference

Re Reynolds Number

P_E Effective power

μ Dynamic viscosity

ρ Density of the Fluid

t Thrust deduction fraction

U Flow velocity of the ROV

P_J Pressure Jump

R_T Total resistance of the ROV

y Distance from first node to the wall

y^+ Dimensionless distance from the first node to the wall

v Kinematic viscosity of the flow

μ_t Turbulent viscosity

X X-axis in co-ordinate system

Y Y-axis in co-ordinate system

Z Z-axis in co-ordinate system

INTRODUCTION

A Remotely Operated Vehicle, abbreviated as ROV, is an important robot carrying out a variety of task underwater. It is supposed to work in deep water and riskier areas. It has significant contribution in the exploration, inspection, maintenance and repair of underwater structures and also in the maritime security. However, we know that underwater environment is very dynamic and can presented disturbances to underwater vehicles in form of currents during their tasks.

The availability of robust commercial computational fluid dynamics software and high speed computing has lead to the increasing use of the computational fluid dynamics for the solution of fluid engineering problems.

For efficiently reason through water, it is wanted to investigate turbulent separated flows around a ROV body using a numerical method, precisely the numerical simulation of the turbulent flow around a fully submerged Remotely Operated Vehicle body using Computational Fluid Dynamics method.

The objective that must be achieved is to investigate the propulsive performances of the moving ROV with ellipsoidal body.

The scopes of this work are:

i. Design a Remotely Operated Vehicle geometry having ellipsoid body, and as propulsion system four ducted propellers, 2 for horizontal displacement and 2 for vertical displacement.
ii. Perform numerical computations of fully submerged stationary ellipsoid for steady-state case.
iii. Use the commercial Computational Fluid Dynamics (CFD) code FLUENT from ANSYS Inc. as tool for numerical computations.
iv. Investigate the effects of the angle of attack on the separation pattern as well as on the hydrodynamic forces and moments.

Computational fluid dynamics method will be used to assess and investigate on ROV's hydrodynamics. Various methods of computational modeling available will be investigated in order to choose one for evaluating hull drag. Various velocities will be applied in order to study the detailed flow structure

In the two first chapters, theoretical backgrounds about ROV, CAD model and CFD technique are given. In the third chapter, Verification and Validation method is applied in to choose the best turbulence model suited for the viscous incompressible flow around ROV body available

in FLUENT for evaluating the hull drag. In the two last chapters, study case and results are shown and discussed. The last part gives the final conclusions and recommendations for the further work.

I. STATE OF ART OF THE REMOTELY OPERATED VEHICLE

1.1. General

The acronym ROV stands for Remotely Operated Vehicle which is an unmanned underwater vehicle widely used in subsea industries. It permits humanity to explore and work in the deep oceans without endangering humans by subjecting them to the hostile deep water environment. It is an underwater robot which is become essential since the new offshore development limited the reach of human divers. ROVs are currently used for a variety of aims such as marine research, retrieval operations, and surveillance system modules.

The ROV is controlled by a user located on the surface vessel and the control mechanism can be either an umbilical cord or via wireless means.

Figure 1.1 shows us a variety of unmanned underwater vehicles that have been made overtime.

Figure1.1: Types of ROV [http://candrayasa.blogdetik.com/2011/08/16/rov/sus_range1/]

In industry, ROVs are designed to move in several different directions and are used to perform short range tasks. The selection of ROV's dimensions is function of its components to install.

Figure 1.2 depicts ROV components which play an important role in its operations.

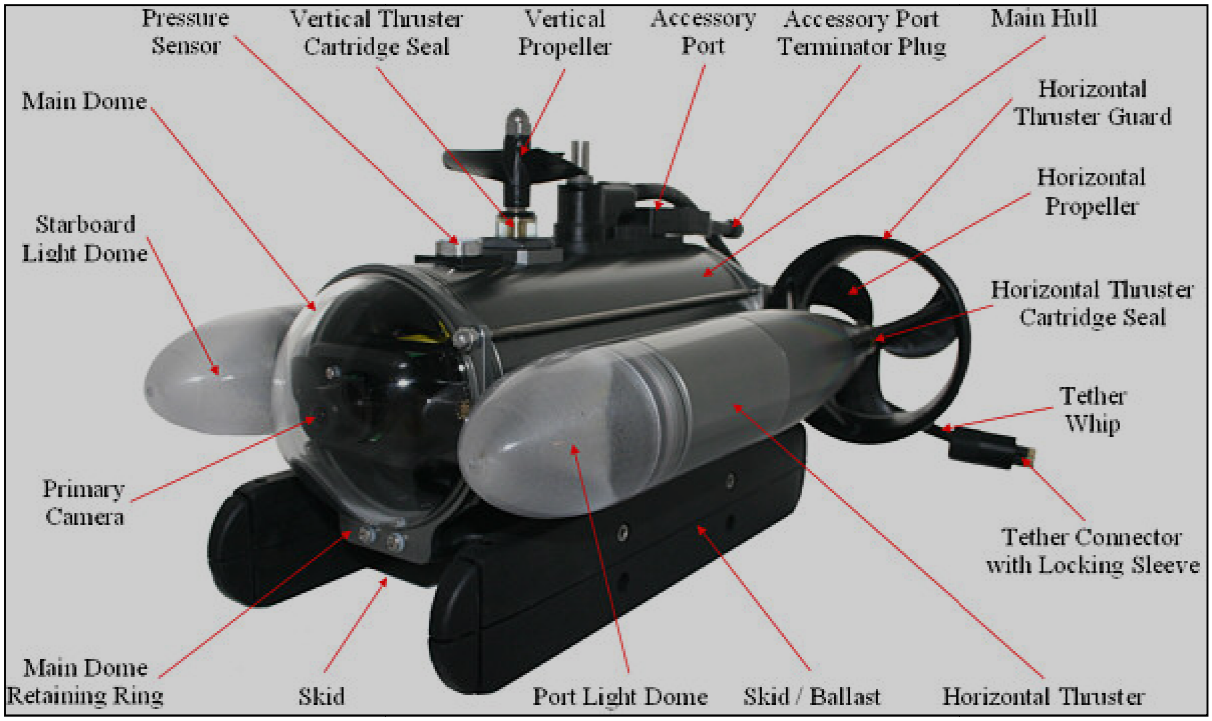

Figure1.2: ROV components
[http://download.videoray.com/documentation/v1_7_0/html/pro4/equip_rov.html]

1.2. ROV geometry

Most ROVs are built inside or around a rectangular frame with a flotation pack on top to provide necessary buoyancy. Our topic emphasizes on ellipsoidal shape taking to account in the design of four ducted propellers; two for vertical displacement and two for vertical displacement. Also the choice of ROV's dimensions of should be similar to existing ROV that is why we had one look in the literature and some manufacturer catalogs.

Following figures and table report some existing ROV with their characteristics.

Figure1.3: ROV LBV300-5
[http://www.seabotix.com/
products/lbv300-5.htm]

Figure1.4: ROV Falcon
[http://www.seaeye.com/
falcon.html]

Figure1.5: ROV Sirio
[http://www.ageotec.com/
cms/index.php/en/products]

Some characteristics of the ROV from catalogs are given below:

Table1.1: ROV'S characteristics from catalogs.

Model / *Characteristics*	LBV300-5	Sirio	Falcon
Length [mm]	520	590	1000
Width [mm]	445	560	600
Height [mm]	260	450	500
Weight in air [kg]	13	40	60
Depth Rating [m]	300	300	300
Speed [m/s]	1.028	> 1.543	> 1.543
Thrusters	2 forward, 2 vertical, 1 lateral	2 horizontal , 2 vertical , 1 lateral	1 forward , 1 vertical, 1 lateral

From literature **R. Gomes, et al**. [5] and **Obreja and Domnisoru** [4] for designing purposes used Remotely Operated Vehicles which have the characteristics below:

Table1.2: Different ROV's characteristics from papers

Model / *Characteristics*	**IES ROV** from R. Gomes, et al [5]	**Mini-ROV** from Obreja and Domnisoru [4]
Length [mm]	1200	500
Width [mm]	670	350
Height [mm]	600	250
Depth [m]	300	30
Shape	Rectangular	Ellipsoidal
Speed [m/s]	> 1.543	1.543
Thrusters	2 forward, 1 vertical, 1 lateral	2 horizontal , 2 vertical

In order to follow the scope of work the hull dimensions of the ROV have been chosen as reported in **Obreja and Domnisoru** [4].

1.3. Numerical modeling of fully submerged Remotely Operated Vehicle (ROV)

Any CFD simulation starts with the realization of the geometry in 2D or 3D with an integrated CFD code or software using Computer-Aided Design software. And then the geometry must be imported in a format readable by software mesh. STEP and IGES formats are most commonly used.

1.3.1. ROV characteristics

As defined in the scope of work, the studied ROV has an elliptical shape meaning that the body is symmetric.

The following table is describing the geometrical characteristics of the ROV.

Table 1.3: Main characteristics of the ROV

Characteristics	Symbol	Value
Length	***L***	500 [mm]
Width	***B***	350 [mm]
Height	***H***	250 [mm]
Mass hull	***M***	5.2 [kg]
Propellers diameter	***d***	50 [mm]
Service speed	***U***	1.5432 [m/s]
Depth rating	***I***	30000 [mm]

1.4. CAD Model

This study starts with the 3D geometry design of the ROV using the CAD software Rhinoceros 3D.

In order to study ROV's resistance and to analyze its propulsive influences in this work, three configurations have been made with the same main characteristics of the ROV:

- The ellipsoidal ROV without channels and propellers called "bare hull";
- The ellipsoidal ROV with channels without propellers called "ROV's hull";
- The ellipsoidal ROV with channels and propellers as defined in the scope of work. It is called "ROV body".

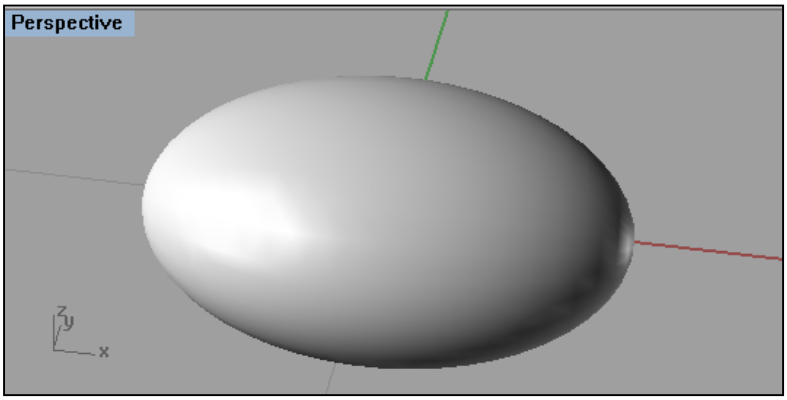

Figure 1.6: Bare hull

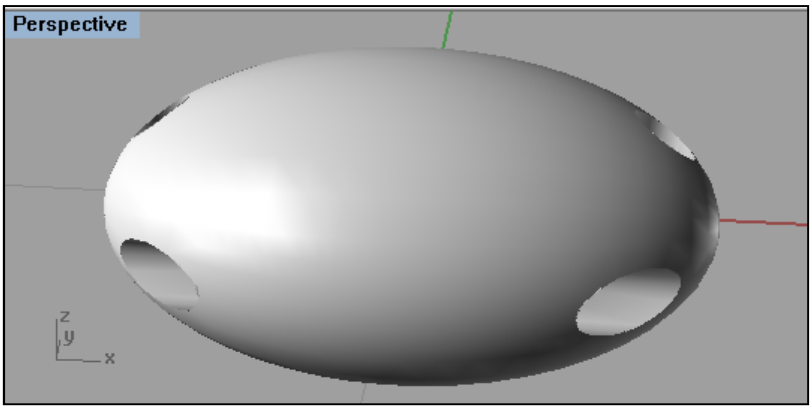

Figure1.7: ROV body

The ROV body is moved by four ducted propellers mounted in two cylindrical channels parallel with x-axis corresponding to the main axis of the ellipsoid and the other two in channels parallel with z-axis. All propellers are considered to have the same characteristics.

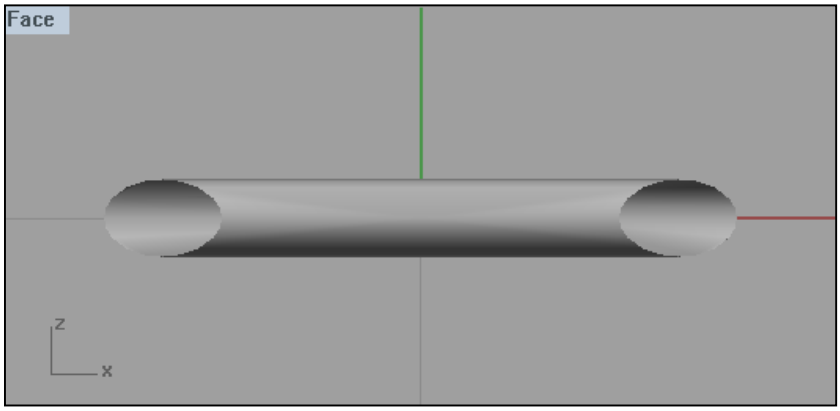

Figure 1.8 : Cylindrical channels

Propeller modeling is based on the principle of the **momentum theory [21]** which consists to reduce the propeller as an actuator disk creating a pressure jump in the flow. Therefore, the four propellers are modeled as actuator disk located at the middle of each channel. Because of the actuator disk force used the detailed geometry of the propeller is not necessary in this study.

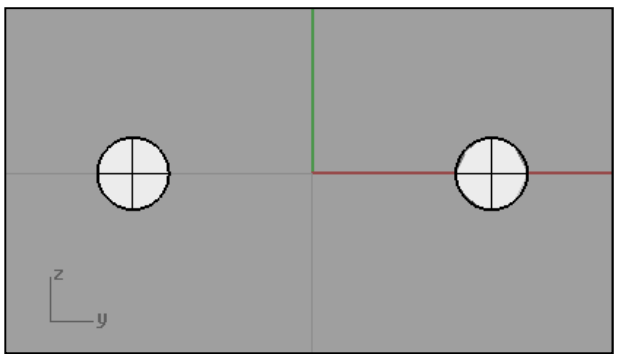

Figure 1.9: Horizontal actuator disks

Practically, it is not necessary to design three different geometries in order to cover these three configurations motioned above because the disk can be set up as interior boundary condition in FLUENT leading to the second configuration about ROV's hull. So, two geometries are enough:

The bare hull presented in *Figure 1.6* and the ROV body shown in *figure 1.7.*

1.5. Flow separation

All bodies travelling through a fluid acquire a boundary layer of fluid around them where viscous forces occur in the layer of fluid near to the body surface. The moving fluid exerts pressure forces normal to the surface and tangential shear forces on the surface.

Turbulent flow is characterized by chaotic movement of the fluid particles. In other words, it is the three dimensional unsteady random motion observed in fluids. A reasonable assessment can be made by calculating the Reynolds number of the local flow conditions. That is given by the following formula:

$$R_e = \frac{\rho U L}{\mu} \tag{1.1}$$

with μ the dynamic viscosity, U the speed, ρ is the density and L the characteristic length.

The presence of boundary layers is the consequence of the fluid viscosity that induces the fluid to be attached to the walls giving a zero speed at wall contact.

By separation, we mean the entire process of departure or breakaway, or the breakdown of boundary layer flow [1].

Flow separation occurs when the boundary layer travels far enough against an adverse pressure gradient that the speed of the boundary layer relative to the object falls almost to zero. The fluid flow becomes detached from the surface of the object, and instead takes the forms of eddies and vortices.

Figure 1.10 shows the separation of the boundary layer for the case circular cylinder.

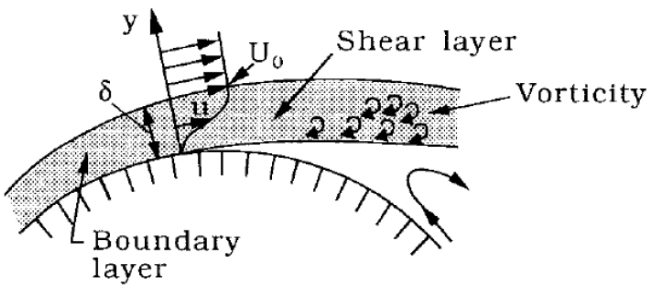

Figure 1.10: Boundary layer separation [11]

In hydrodynamics, flow separation results in a drag increase, significant lift loss and unsteady fluctuations [6]. That is why much effort and research has gone into the design of hydrodynamic surfaces which delay flow separation and keep the local flow attached for as long as possible in order to reduce the energy consumption in submersibles through the propulsion system.

1.6. ROV's hydrodynamics

ROV's hydrodynamics play an important role into the investigation of its propulsive performance. Propulsion features of a submerged body are found by the performance of the body and the propeller system, in our context by the performance of the ellipsoidal ROV with its four ducted propellers, two for vertical displacement and others for the horizontal displacement.

The ROV's resistance is affected by the induced velocity field of propellers and the ROV body affects the propellers performance through its wake. That is why, it is necessary to study ROV resistance problem which is linked to the power prediction leading to a better choice of the required engines which can optimize fuel consumption.

Flows of fluid over submerged bodies such as ROV body involve external flows which are typified by freely growing boundary layer surrounded by an outer region. Forces imparted by this moving fluid can be described in terms wall shear stresses due to viscous effects and normal stresses due to the pressure.

The lift force is the component that acts normal to the flow direction.

The component of the resultant pressure and shear forces in the flow direction is so-called drag. The total drag force is the sum of the pressure forces called *pressure drag* and the wall shear stress called *friction drag* [3]. It acts on the ROV body to slow it down.

In practice it is not easy to separate their values and the calculation way is by integrating over the entire surface of body.

The dimensionless force coefficients are given by:

$$C_D = \frac{Drag}{\frac{1}{2}\rho U^2 A} \tag{1.2}$$

where ρ is the density, L the characteristic length and A the characteristic area.

Similar to drag coefficient, the lift and moment coefficients may be computed as:

$$C_L = \frac{Lift}{\frac{1}{2}\rho U^2 A} \tag{1.3}$$

$$C_M = \frac{Moment}{\frac{1}{2}\rho U^2 AL} \tag{1.4}$$

The pressure coefficients are defined as

$$C_p = \frac{\Delta p}{\frac{1}{2}\rho U^2} \tag{1.5}$$

Where Δp is the difference of pressure between ROV's surface and far fields.

The power required to tow the ROV without propeller system is the effective power P_E given by:

$$P_E = R_T * U \tag{1.6}$$

where U is the speed of the ROV.

One influence factor of the propeller on the hull is the thrust deduction fraction *t* which is the normalized difference between propellers thrust *T* and the total hull resistance R_T defined by

$$t = 1 - \frac{R_T}{T} \tag{1.7}$$

To understand some basic concepts of propeller flows, actuactor disk theory is used. Propellers are considered as actuator disk and generate a pressure jump in the flow. The created thrust is expressed in propeller plane as increased velocities and is uniformly distributed over the disk.

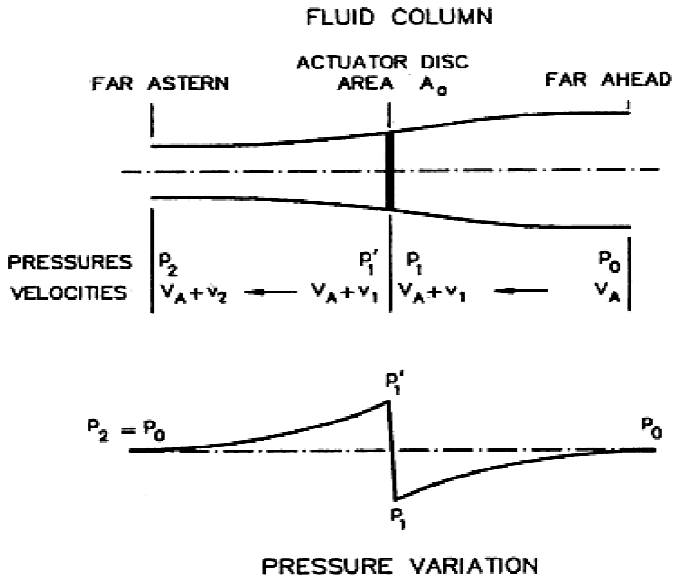

Figure 1.11: Action of an actuator disk in the axial momentum theory [22]

The corresponding pressure jump is determined by:

$$P_J = \frac{T}{A_0} \tag{1.8}$$

where A_0 is the cross-sectional area of the disk.

1.7. Published work

In the knowledge of the authors, excepting [6], there are few literatures concerning the CFD analysis on the elliptical ROV. But some published papers used CFD of whole submersibles for estimation of drag force for design purposes for instance [5], [6], [7] and [8], while the other emphasizes on the separation point at the airfoil surface [9].

Turbulent separated flows are a complex behavior described by **Roger L. Simpson** [5] for best understanding of this physical phenomenon.

I. Shukry et al [9] concerns a numerical analysis includes modeling of separation flow of a two-dimensional, incompressible, steady and turbulent flow around NACA 0012 airfoil. The study includes the numerical solution of the continuity and momentum equations with the two equations of the k-$\mathcal{E}$ turbulence model. Flow separation and its effects under different flow conditions were described. Separation point at the airfoil surface is predicted at high angles of attack. It is found that increase the angle of attack will lead to increases all of separation occurrence, recirculation, and reversed flow also, pressure, lift and drag coefficients are highly influenced by the angle of attack and the Reynolds number before stall angle. The computations were performed for different Reynolds numbers and different angles of attack. The lift coefficient increases with increase of Reynolds number until the stalling angle occurs. This paper shows that in the case of airfoil there is effectively a link between the angle of attack and the separated flow.

Also **J. L. Montagne** [10] noticed *when the submersible moves at sufficiently large angles of attack, these phenomena are characterized by the separation of the boundary layer vorticity from the body surface.*

R. Sakthivel et al [7] mentions after using the CFD approach that 3D flow simulation can be used to study the complex flow behavior over underwater bodies at higher angle of attacks. Taking underwater hull at a Reynolds number of $2.09*10^6$, he shows that the nonlinear k-Ɛ model performs more well 3D turbulent flows with flow separation and reattachment than the standard k-Ɛ turbulent model particularly at higher angle of attack. It is found the key parameter in flow variable at higher of angle of attack is the circumferential pressure gradient.

Y. Eng et al. [8] joins CFD results and basin tests in order to cover a lot of different aspects of the added mass and drag coefficient study of a scaled down model of ROV. A new free decay test has been used to find the added mass and drag coefficient. And the results are compared with simulation results got from established CFD program. This approach can be scaled up drag coefficients for any ROV.

G. Iaccarino et al. [13] investigates the accuracy of Reynolds averaged Navier Stokes (RANS) turbulence models in predicting complex flows. The unsteady flow around square cylinder and over a wall-mounted cube are simulated and compared with experimental data.

The study shows that unsteady RANS provides good quantitative and qualitative agreement with experimental data when the flow is not statistically stationary.

It mentions *that none of the previously published numerical predictions obtained by steady-state RANS produced a good match with experimental data* cause of the of coherent vortex shedding in this flow.

Turbulent separation flows around ellipsoids of various aspect ratios are investigated using a numerical method by **Ungureanu and Lungu** [6]. Reynolds averaged equations for continuity and momentum are solved by cell centered finite volume method for the primitive variables to describe the 3D turbulent incompressible flow. Five different shapes were considered and only three geometries and two angles of attack, which correspond to the movement along the main axes of the ellipsoid. However, some restriction imposed by the minimum space required on board, led the authors to choose the 0.5x0.35x0.25m hull as mentioned **Obreja and Domnisoru [4]**.

Both steady and unsteady flow cases were studied but the unsteady computation has been carried and it was found that the separated flow around the body results in a total drag increase, significant lift loss, and unsteady fluctuations.

2. COMPUTATIONAL FLUID DYNAMICS METHOD

2.1. Procedure

Computational Fluid Dynamics or CFD is a part of fluid mechanics which uses numerical methods and algorithms to solve and analyze problems relating to fluid flows by a set of algebraic equations by using of digital computers.

Turbulent flow separation is a physical phenomenon which can be simulated numerically thanks to CFD Method. It is the physical problem of this study before setting up the

mathematical model. This flow should be simulated with the Navier-Stokes equations and the basic procedure to perform numerical simulation of fluid flows requires a discretization step in which the continuous governing equations and the domain of interest are changed into a discrete set of algebraic relations valid in a finite number of location.

The general procedure [15] is given by the following steps:

- Define the modeling goals;
- Create the model geometry and grid;
- Set up the solver and physical models;
- Compute and monitor the solution;
- Examine and save the results;
- Consider revisions to the numerical or physical model parameters.

However, when performing numerical analysis, it is important to generate less numerical errors.

The characteristics of the computer used are reported in the *table 1.3* and the solver recommended in Computational Fluid Dynamics simulation is Fluent 6.3.

Table1.4: Characteristics of the computer used

Processor	Intel® core ™ i5-2400, 3.10 GHz
RAM	4.00 GB
System type	64-bit operating system

2.2. Mathematical model

The beginning of any numerical simulation method is the mathematical model after defining clearly the physical problem. The mathematical model means the set of partial differential or integro-differential equations and boundary conditions. These equations called **Navier-Stokes equations** are fundamental for the fluid flow. The governing equations are the continuity, the momentum and energy equations representing the conservation laws of physics.

- Fluid mass is conserved
- The rate of change of momentum equals the sum of the forces on a fluid particle

- The rate of change of energy is equal to the sum of the rate of heat addition to and the rate of work done on a particle.

2.2.1. Continuity equation

The change of mass in a control volume is equal to the mass that enters through its faces minus the total mass leaving its face. This equation is based on the law of conservation of mass. Continuity equation, for incompressible flow with the velocity vector expanded as *V = (u,v,w),* is given by

$$\frac{\partial u}{\partial x}+\frac{\partial v}{\partial y}+\frac{\partial w}{\partial z}=0 \tag{2.1}$$

2.2.2. Momentum equation

Momentum equation results from Newton's Law of Motion ensuring that the rate of change of momentum of the fluid particles is equal to the total force due to surface stresses and body forces acting in an aligned direction of a chosen coordinate axis.

$$\frac{\partial u}{\partial t}+(u.\nabla)u=-\frac{1}{\rho}\nabla p+F+\frac{\mu}{\rho}\nabla^2 u \tag{2.2}$$

where p, ρ and F are respectively the pressure, the fluid density and the external force per unit mass.

2.2.3. Energy equation

The energy equation describes the transport of heat energy through a fluid and its effects and is based on the first law of thermodynamics.

$$\frac{\partial \mathrm{E}}{\partial t}+\nabla.\big(u(\mathrm{E}+p)\big)=0 \tag{2.3}$$

With $\mathrm{E}=\rho e+\frac{1}{2}\rho(u^2+v^2+w^2)$ the total energy per unit volume and e the internal energy per unit mass for fluid.

2.3. Discretization Methods

The next step after setting up the mathematical model is to choose the discretization method. These methods are classified in four main families:

- Finite Differences Methods
- Finite Element Methods
- Spectral Methods
- Finite Volumes Methods

The discretization of one physical problem with Navier-Stokes equations requires the discretization of the fluid domain and the discretization of equations which are used under integral form for each cell of the domain [14].

For this study, the commercial CFD code FLUENT has been recommended to perform numerical computations. This software is able to perform incompressible and compressible modeling of both laminar and turbulent fluid flows, and is also based on the finite volume method where computational domain is discretized into a finite set of control volumes. The steady-state conservation equation for transport of a scalar quantity ϕ to be solved is:

$$\oint \rho\phi\vec{v}.d\vec{A} = \oint \Gamma_\phi \nabla\phi.d\vec{A} + \int_V S_\phi dV \quad (2.4)$$

Where ρ is the density, $\vec{v}$ the velocity vector, $\vec{A}$ the surface area vector, V the control volume, S_ϕ the source of ϕ per unit volume, $\nabla\phi$ the gradient of ϕ and Γ_ϕ the diffusion coefficient for ϕ.

2.4. Numerical resolution approach for turbulent flow

In principle, turbulence flow is described by the Navier-Stokes equations which are the governing equations of fluids. After discretization, these equations have to be solved by one technique of resolution.

For turbulent flow modeling, there are several approaches of resolution in current CFD software according to the complexity of the simulation. Some of them are:

- Direct Numerical Simulation which is probably more accurate but costly and not use in industry cause of time consuming;
- Large Eddy Simulation adapted for largest scale motion s of the flows;
- Detached Eddy simulation, available for the unsteady separated region and able to solve shear layer through RANS;
- Reynolds-Average Navier-Stokes approach available for steady state simulation or transient situation leading to a set of partial differential equations.

Most widely used approach for practical purposes is Reynolds-Average Navier-Stokes method thanks to its advantage to apply an averaging procedure.

2.4.1. Reynolds Average Navier-Stokes

This resolution approach eliminates turbulence structures by averaging procedures applied to Navier-Stokes equations which are decomposed in the mean and fluctuating components. For incompressible flows and velocity components:

$$u = \bar{u}_i + u_i' \tag{2.5}$$

Where $\bar{u}_i$ and u_i' are respectively the mean and fluctuating velocity components ($i = 1,2,3$).

Likewise, for the pressure and other scalar quantities:

$$\phi = \bar{\phi} + \phi' \tag{2.6}$$

Where ϕ denotes a scalar such as pressure, energy, etc…

And the time averaging velocity component is given by

$$\bar{u}_i = \frac{1}{T}\int_0^T u dt \tag{2.7}$$

Substituting expressions into Navier-Stokes equations for time averaging yields Reynolds-averaged Navier-Stokes equations written below.

$$\frac{\partial u_i}{\partial x_i} = 0 \tag{2.8}$$

$$\frac{\partial \bar{u}_i}{\partial t} + \bar{u}_j \frac{\partial \bar{u}_i}{\partial x_j} = -\frac{1}{\rho}\left(\frac{\partial \bar{p}}{\partial x_i}\right) + \frac{\partial}{\partial x_j}\left(\nu \frac{\partial \bar{u}_i}{\partial x_j} - \overline{u_i' u_j'}\right) \tag{2.9}$$

where *p*, ρ and *v* are respectively the pressure, fluid density and kinematic viscosity of the flow. The unknown term $\overline{u_i' u_j'}$ is Reynolds stress representing the effect of the turbulence, must be modeled in order to close *equation 2.8.* Therefore turbulence modeling consists to define the Reynolds stress in terms on known quantities and the main turbulence model assumptions are [14]:

- Reynolds stress transport models
- Boussinesq hypothesis giving simple relationship between Reynolds stresses and velocity gradients through the eddy viscosity.

$$\overline{u_i' u_j'} = -\mu_t\left(\frac{\partial \bar{u}_i}{\partial x_j} + \frac{\partial \bar{u}_j}{\partial x_i}\right) + \frac{2}{3} k \delta_{ij} \tag{2.10}$$

The challenge is how to express the turbulent viscosity among various models classified in terms of number of transport equations solved in addition to the RANS equations.

2.5. RANS Turbulence Models available in FLUENT

According to [15], for computing turbulent flows, RANS models offer the most economic approach and are suitable for many engineering applications. These models provide an Eddy-Viscosity to determine the Reynolds Stresses and simplify the problem to the solution of the additional transport equations.

RANS turbulence models available in FLUENT are mentioned below:

- Spalart-Allmaras One-Equation Model;
- k-ε Models;
- k-ω Models;
- Reynolds Stress Models (RSM).

2.5.1. Spalart-Allmaras One-Equation Model

The Spalart-Allmaras model is a one-equation model used to approximate the Reynolds Stresses in Reynolds average Navier-Stokes equations. It solves a modeled transport equation for kinematic eddy viscosity. The transport equation is defined by [15]:

$$\frac{\partial}{\partial t}(\rho\tilde{v}) + \frac{\partial}{\partial x_i}(\rho\tilde{v}u_i) = G_v + \frac{1}{\sigma_{\tilde{v}}}\left[\frac{\partial}{\partial x_j}\left\{(\mu + \rho\tilde{v})\frac{\partial\tilde{v}}{\partial x_j}\right\} + C_{b2}\rho\left(\frac{\partial\tilde{v}}{\partial x_j}\right)^2\right] - Y_v + S_{\tilde{v}} \qquad (2.11)$$

where

- $\tilde{v}$ is the transported variable considered as the turbulent kinematic viscosity except in the near-wall region;
- G_v is the production of the turbulent viscosity;
- Y_v is the destruction of turbulent viscosity that occurs in the near-wall region due to wall blocking and viscous damping;
- C_{b2} and $\sigma_{\tilde{v}}$ are the constants and ν the molecular kinematic viscosity;
- $S_{\tilde{v}}$ is a user-defined source term.

Turbulent viscosity μ_t is obtained from

$$\mu_t = \rho\tilde{v}f_{v1} \qquad (2.12)$$

With the viscous damping f_{v1} given by

$$f_{v1} = \frac{\left(\frac{\tilde{v}}{v}\right)^3}{\left(\frac{\tilde{v}}{v}\right)^3 + C_{v1}^3} \qquad (2.13)$$

The Spalart-Allmaras model has been shown to give an accurate prediction of turbulent flow with adverse pressure gradients. This model is easy to implement on the structured and unstructured grids and also numerically very stable.

2.6. Nearwall modeling

Inasmuch as walls are the main source of turbulence and mean vorticity, it is necessary to perform an accurate representation of the flow in the near-wall region where boundary layer is created.

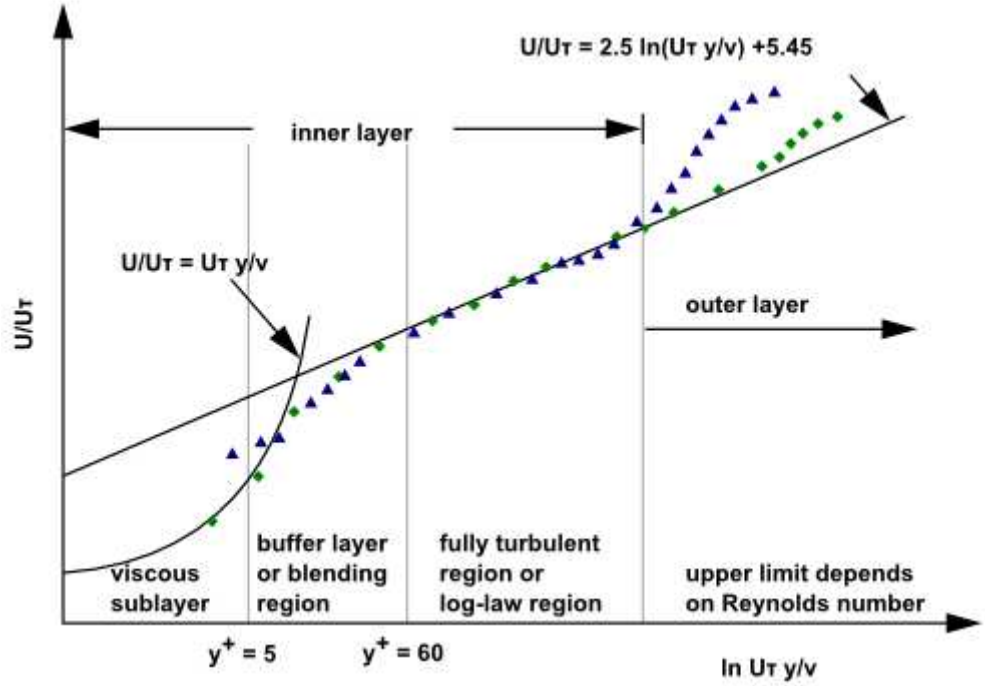

Figure 2.1 : Subdivision of the Near-Wall Region [15]

Experiments and mathematical analysis have shown that the near-wall region can be subdivided into three layers:

- Viscous sublayer where the flow is almost laminar and the viscosity plays an important role in momentum and mass transfer.
- Fully-turbulent layer where turbulent plays a major role.
- Finally, buffer layer, an interim region between viscous sublayer and Fully-turbulent layer where the effect viscosity and turbulence are equally dominant.

There are two approaches to modeling the near-wall region and both are available in Fluent:

- Wall function approach, where the flow near the wall is not solved, but determined by using semi-empirical formulas in order to bridge the viscosity-affected inner region between the wall and the fully-turbulent region.
- Near-wall model approach, modifying turbulence models in order to resolve with a mesh all the way to the wall, the viscosity-affected region.

To solve turbulent problem in this study, Near-wall model approach will be used for the modeling of the near-wall region. That requires a minimum spacing between grid elements in order to correct model the viscous sublayer in the boundary layer. The estimation of the first cell size y is based on the ITTC standard method [16] and given in function of the non-dimensional wall distance y^+ (y^+at the wall adjacent cell should be on the order of $y^+ = 1$ [15]), and the local Reynolds number R_e of the ROV.

The expression for y^+ is

$$y^+ = \rho u_T y/\mu \tag{2.18}$$

where u_T is the velocity friction, defines as $\sqrt{\tau_w/\rho}$

$$y = \frac{y^+ L}{R_e\sqrt{C_f/2}} \tag{2.19}$$

$$C_f = \frac{0.075}{(\log_{10} R_e - 2)^2} \tag{2.20}$$

where L is the length of ROV and C_f the skin friction coefficient.

The Reynolds number corresponding to the length of the ROV is equal $7.68 * 10\text{^}5$. Therefore, the value of the first cell thickness that must be introduced during the grid generation procedure is y =1.3E^{-5} m.

2.7. Grid generation

The grid or mesh is the discrete representation of the geometry of the problem, designating the cells over which the flow is solved. It has great influence on the solution accuracy, the rate of convergence and the CPU time required. Mesh generation is a very important step in a CFD analysis because of its influence on computations.

For this study, the process of meshing is performed using GAMBIT software.

Several kinds of grid topology are available:

- Structured grid identified by regular connectivity;
- Unstructured grid identified by irregular connectivity with no constraints on cell layout and no i, j, k grid index;

- Hybrid grid containing a mixture of structured portions and unstructured portions.

In order to capture all important flow features, the grid must be fine.

2.8. Numerical schemes

Navier-Stokes equations show linear dependence of velocity on pressure and vice-versa. This relationship between them is called velocity pressure coupling. Several methods are available in order to realize this velocity pressure coupling:

- SIMPLE
- SIMPLEC
- PISO
- Coupled

Cause of the steady-state problem to solve in this work, SIMPLE algorithm will be used meaning the velocity field is determined by solving the momentum equation, and the pressure gradient is obtained using the pressure distribution from the previous iteration.

2.9. Body forces

As the objective of the study is to investigate the propulsive performances of the moving ROV which is linked to resistance, it is necessary to understand how the commercial code FLUENT computes the different forces and moment acting on the ROV body.

2.9.1. Forces and Moment Reports

After computations, the commercial code FLUENT is able to provide forces and moment reports in text file or others. According to this software [15], the total force component along one specified forces vector $\vec{a}$ acting on a body surface is computed as:

$$\underbrace{F_a}_{\textit{Total force component}} = \underbrace{\vec{a}.\overrightarrow{F_p}}_{\textit{Pressure force component}} + \underbrace{\vec{a}.\overrightarrow{F_v}}_{\textit{Viscous force component}} \quad (2.1)$$

Where $\overrightarrow{F_p}$ and $\overrightarrow{F_v}$ are the pressure force vector and the viscous force vector.

The net pressure force vector is calculated as the vector sum of the individual force vectors for each cell face:

$$\overrightarrow{F_p} = \sum_{i=1}^{n} (p - p_{ref}) A\hat{n} \tag{2.2}$$

$$\overrightarrow{F_p} = \sum_{i=1}^{n} pA\hat{n} - p_{ref} \sum_{i=1}^{n} A\hat{n} \tag{2.3}$$

Where *n, A* and $\hat{n}$ are the number of faces, the area of the face and the nit normal to the face respectively.

The total moment vector about one specified center *O* is given by:

$$\underbrace{\overrightarrow{M_O}}_{\text{Total moment}} = \underbrace{\vec{r}_{OB} * \overrightarrow{F_p}}_{\text{Pressure moment}} + \underbrace{\vec{r}_{OB} * \overrightarrow{F_v}}_{\text{Viscous moment}} \tag{2.4}$$

where $\vec{r}_{OB}$ is the vector from the specified moment center *O* to the force origin *B.*

3. VERIFICATION AND VALIDATION

The ability of the computational Fluid Dynamics to provide a numerical solution is important but no enough because of its credibility as an Engineering tool which depends on the quantification of the error / uncertainty of the results. This process is known in the literature as Validation and verification (V&V).

Roache, P. J, [23] adopts the succinct description of verification as “solving the equation right,” and of validation as “solving the right equations.”

For this study, the commercial CFD code FLUENT has been used to perform numerical computations. This software provides various turbulence models. The choice of turbulence model depends on many considerations like the physics of the flow, available computational resources, amount of the time available for the simulation and the establish practice for a specific class of problem, etc.

To make one appropriate choice of model for our simulation, Verification and Validation method from **ASME V&V 20-2009 [17],** will be applied in order to determine the model which provides less discretization error meaning the suitable one for simulating turbulent flow around ROV body. Also this method will help us to validate computations during this study.

3.1. Verification and Validation methodology

ASME V&V 20-2009 [17] procedure consists to compare simulation results or solutions with an experimental data for variables of interest at a specified set of conditions. The error δ of a simulation or experiment is the difference between calculated and measured value and the truth.

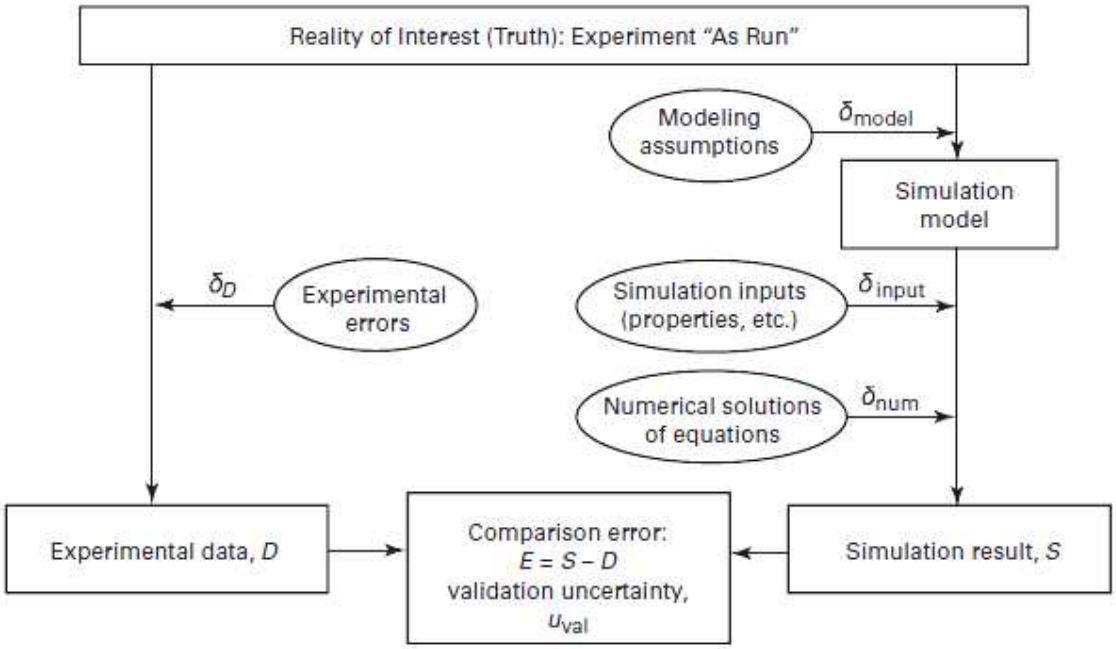

Figure 3.1 : Overview of the validation process with sources of error [17]

The validation comparison error *E* is defined as:

$$E = S - D \tag{3.1}$$

where S is the simulation result and D the experimental data.

The error in the simulation result is the difference between *S* and the true value *T*:

$$\delta_S = S - T \tag{3.2}$$

Also the error in the experimental value D is:

$$\delta_D = D - T \tag{3.3}$$

Using *equations 3.2* and *3.3*, the expression of the validation comparison error *E* becomes:

$$E = (T + \delta_S) - (T + \delta_D) \tag{3.4}$$

$$E = \delta_S - \delta_D \tag{3.5}$$

Three kinds of error can be considered when performing numerical simulation:

- The error δ_{SM} due to modeling assumptions;
- The error δ_{SN} due to numerical solution of equations;
- The error δ_{SIn} in the simulation results due to error in the simulation input parameters.

Hence the numerical error can be defined as:

$$\delta_S = \delta_{SM} + \delta_{SN} + \delta_{SIn} \tag{3.6}$$

And the associated numerical uncertainty is

$$U_S^2 = U_{SM}^2 + U_{SN}^2 + U_{SIn}^2 \tag{3.7}$$

The modeling error δ_{SM} is deduced from equations *3.4-3.5*

$$\delta_{SM} = E - (\delta_{SN} + \delta_{SIn} + \delta_D) \tag{3.8}$$

F. Stern et al. [18] defines the validation uncertainty U_{VAL} as

$$U_{VAL}^2 = U_E^2 - U_{SM}^2 = U_{SN}^2 + U_{SIn}^2 + U_D^2 \tag{3.9}$$

and characterizes an interval in which falls the modeling error $\boldsymbol{\delta_{SM} \in [E - U_{VAL}; E + U_{VAL}]}$.

F. Stern et al [18] and **Roache, P. J** [23] recommended that the certainty level of the solution should be 95% in the ship hydrodynamics.

3.1.1. Comparison error vs. validation uncertainty

As defined above, the validation comparison error *E* is the difference between simulation results and experimental data.

If $|E|$ is greater than or equal to U_{VAL}, the modeling error $\boldsymbol{\delta_{SM}}$ is probably similar to $|E|$. There is information about the need to improve the model;

If $|E|$ is less than U_{VAL}, the modeling error $\boldsymbol{\delta_{SM}}$ is smaller than the noise that originated by the numerical, experimental and input parameters uncertainty.

3.1.2. Numerical uncertainty

Numerical errors and uncertainties can be based on these three parameters:

- Round-off errors, δ_R;

Round-off errors are due to the finite precision of computers. They can be ignored if it is used double precision solver or 64 bits architecture machines, which allows the representation of numbers by fifteen characters compared to only seven in simple precision. For this reason all numerical computations were performed with the double precision solver.

- Iterative errors, δ_I;

Iterative errors are from the equations nonlinearity solved by numerical methods and can be eliminated if the solution converges to machine precision.

According to **Roy et al.** [19] and **Eça., Hoekstra et al.** [20]**,** iterative errors can be neglected if they are two or three order of magnitude smaller than the discretization errors.

- Discretization errors, δ_G.

Discretization errors are a consequence of the transformation of the continuum equations into a system of algebraic equations.

ASME V&V 20-2009 [17] defines five step procedures in order to determine discretization errors and its associated uncertainty or fine convergence index abbreviated GCI.

The procedure is the following:

- Define a representative grid size *h* for three-dimensional calculations.

For unstructured grid we have:

$$h = \left[\frac{1}{N}\sum_{i=1}^{N}(\Delta V_i)\right]^{1/3} \tag{3.10}$$

where *N* is the total number of cells used for computations and ΔV_i the volume of the i^{th}cell.

- Select three significantly different sets of grids (fine h_1, medium h_2 , and coarse h_3)

and run simulations to obtain the values of key variables ϕ which are drag forces for the present work. But before we have to choose the grid refinement factor *r* greater than 1.3 that is based on experience. It allows to establish different size of grid h_1, h_2 and h_3.

Generally, the grid refinement factor can be also calculated by

$$r = \frac{h_{coarse}}{h_{fine}} \tag{3.11}$$

For this study the value of the grid refinement factor is kept constant in order to set these three types of grid ($r_{21} = r_{32}$).

- Determine the apparent order p for $h_1 < h_2 < h_3$, $r_{21} = \frac{h_2}{h_1}$ and $r_{32} = \frac{h_2}{h_3}$

$$p = \frac{1}{\ln(r)}\left|ln\left|{}^{\varepsilon_{32}}/_{\varepsilon_{21}}\right| + q(p)\right| \tag{3.12}$$

$$q(p) = ln\left(\frac{r_{21}^{p} - s}{r_{32}^{p} - s}\right) \tag{3.13}$$

$$s = 1.sign\left({}^{\varepsilon_{32}}/_{\varepsilon_{21}}\right) \tag{3.14}$$

$$\text{With} \qquad \varepsilon_{32} = \phi_3 - \phi_2 \tag{3.15}$$

$$\varepsilon_{32} = \phi_2 - \phi_1 \tag{3.16}$$

- Calculate the extrapolated values from

$$\phi_{ext}^{21} = (r_{21}^{p}\phi_1 - \phi_2)/(r_{21}^{p} - 1) \quad (3.17)$$

Similarly ϕ_{ext}^{32} can be calculated.

- Compute the discretization error with:

$$\delta_G = \frac{e_{ext}^{21}}{r_{21}^{p} - 1} \quad (3.18)$$

Where the extrapolated relative error is

$$e_{ext}^{21} = \left|\frac{\phi_{ext}^{12} - \phi_1}{\phi_{ext}^{12}}\right| \quad (3.19)$$

The discretization uncertainty (U_G) or the fine grid convergence index (GCI):

$$U_G = GCI = F_S|\delta_G| \quad (3.20)$$

where F_S is the factor of safety and according to

$$F_S = 1.25 \text{ if } 0.5 < p < 3.5,\ p > 4.5$$

$$F_S = 3 \text{ if } 3.5 < p < 4.5,\ p > 0.5$$

The numerical error is expressed by:

$$\delta_{SN} = \delta_R + \delta_I + \delta_G \quad (3.21)$$

and the associated uncertainty equation is:

$$U_{SN}^2 = U_R^2 + U_I^2 + U_G^2 \quad (3.22)$$

For simulating flows around the ROV body, the numerical error δ_{SN} will be based on the discretization errors δ_G because of double precision solver used and the reached convergence criterion.

3.2. Verification

3.2.1. Simulation of the flow around the fully submerged bare hull

Numerical simulation of flow around the bare hull described in *section1.4* has been performed in order to choose the turbulence model that provides less discretization error by applying Validation and Verification method from ASME V&V 20-2009 [17].

Validation and Verification method from **ASME V&V 20-2009** [17] is recommended by **Celik, I. B., et al** [2] for discretization error estimation and is used in order to access the accuracy of our computational simulation and find the model of turbulence suited to the simulation around the ROV body.

3.2.1.1. Domain of simulation

The computational domain is the area of interest for the simulation of the flow around the ROV. If it is too small, it may affect the results of the simulation through the surrounding boundaries.

In order to ensure that there is no effect from the surrounding boundaries, the computational domain has been made by scaling each radius of the ROV by ten. Therefore the computational domain has ellipsoidal shape like the ROV, and its size is 10L*10B*10H.

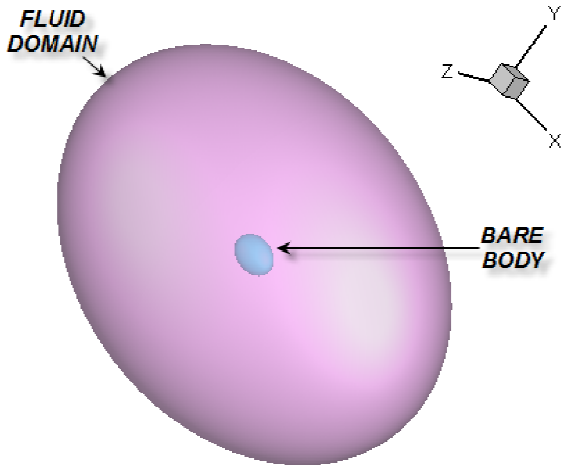

Figure 3.2: Perspective view of the computational domain, bare hull

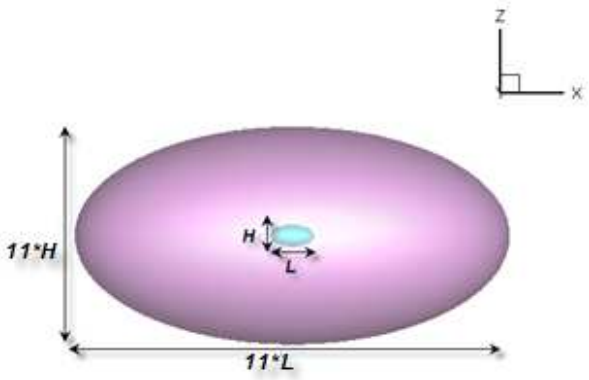

Figure 3.3: Right view
of the computational domain, bare hull

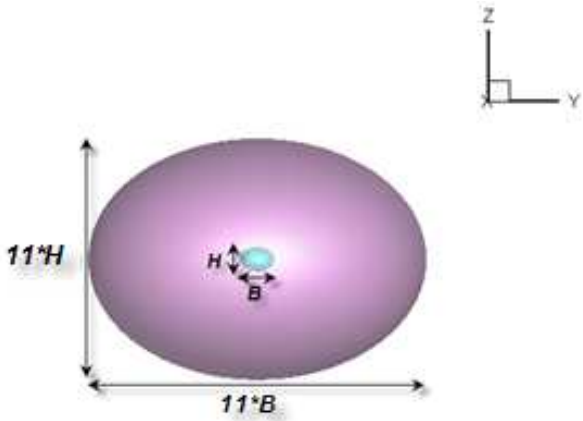

Figure 3.4: Back view of the
computational domain, bare hull

3.2.1.2. Mesh

Both structured and unstructured grids have been generated in this simulation. The domain surface and the bare body surface have the same kind quadrilateral elements (Pave). In order to provide the availability for controlling boundaries layers, mapped hexahedral volume mesh is employed inside the fluid domain. As determined in *section 2.6*, the value of the wall distance introduce for modeling boundary layer is equal to $1.3E^{-5}$ m with a growth ratio of 1.2. All grids have been performed using the software GAMBIT and the figures below present grids from computational domain for fine case.

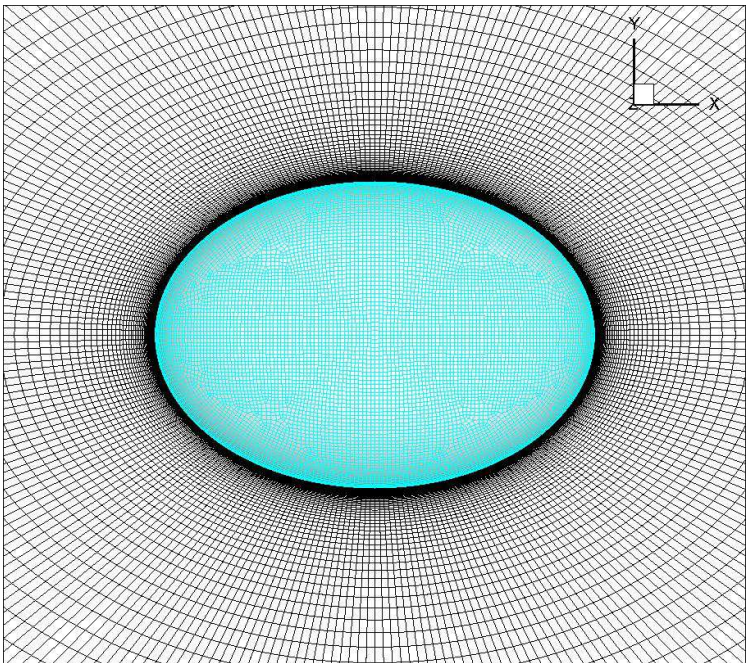

Figure 3.5: Grid around bare hull

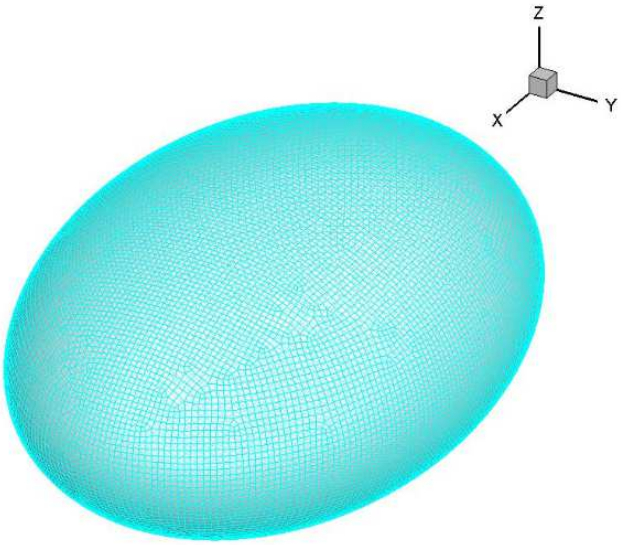

Figure 3.6: Grid on the bare hull

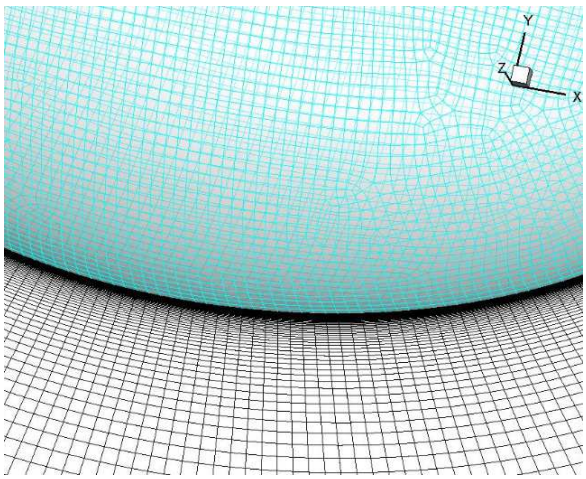

Figure 3.7: Bare hull boundary layer

In order to apply the **ASME V&V 20-2009 [17]** errors discretization procedure, three significant grids have been generated with constant coarsening ratio $r_{21} = r_{32} = \sqrt{2}$ and the same near wall distance y^+=1, so that the steady-state solver perform the boundary layer in the same conditions.

Table 3.1: Grid generation conditions

Grids	**Fine 1**	**Medium 2**	**Coarse 3**
Number of cells [N]	1976800	698904	247100
Mesh size[hi]	0.02261	0.03197	0.04521
Near wall	$y^+ = 1$	$y^+ = 1$	$y^+ = 1$
Grid ratio	r21=	1.41 r32=	1.41
Domain volume	22.83772	22.83772	22.83772

3.2.1.3. Boundary and initial conditions

The computational domain is divided into many parts in order to set boundaries conditions:

- Inlet defined as velocity inlet;
- Outlet as outflow boundary condition ;
- Bare body defined as wall (No-slip boundary condition).

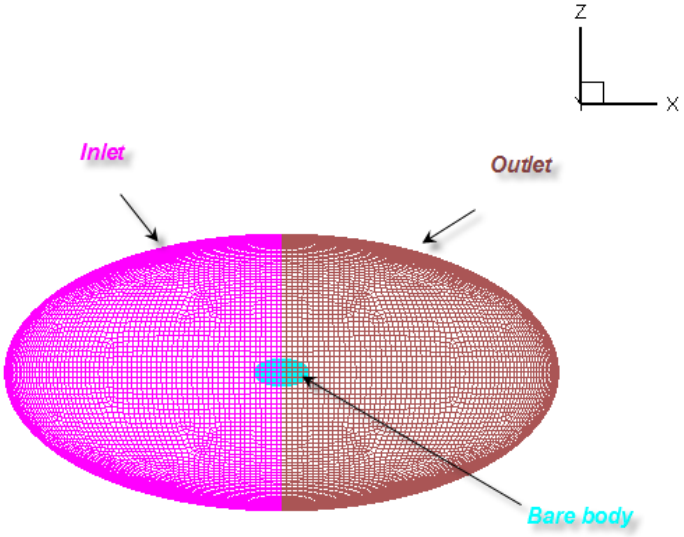

Figure 3.8: Boundary condition for bare hull

The velocity inflow condition is imposed according to the operating ROV speed at theupstream. Hence, longitudinal uniform velocity of 1.5432 m/s is introduced at the inlet.
Outflow boundary condition is used for the downstream and outer boundaries.
The turbulent length scale is equal to 0.035 m, meaning 7% of the ROV's length and the turbulent intensity set up to 3% for the velocity inlet boundary condition.
No-slip boundary condition with a Neumann pressure has been applied on the ROV surface defined as wall meaning there is no fluid penetration on ROV's surface and the fluid is at rest there.

3.2.1.4. Solver set up

The commercial CFD code FLUENT is used to simulate turbulent flow in this study.
Numerical computations were performed at Reynolds number $Re = 7.68 * 10\text{^}5$ with the double precision steady-state solver. Spalart-Allmaras turbulence model is employed for the Reynolds stress of the turbulent flow computation at zero angle of attack. The convergence criterion is set as 10^{-4} for momentum, continuity, kinematic energy and dissipation rate. SIMPLE algorithm has been used for pressure velocity coupling. Second order upwind scheme is used for momentum and turbulence quantities. The reference values used for computing total forces (as described *in section 2.9.1*) are presented in *appendix B*

3.2.2. Results

The discretization errors are computed following ASME method [17]. Round-off and iterative errors were neglected due to double precision solver used and iterating until machine precision was reached. Results are presented in the table 3.2

Table 3.2: Discretization error and uncertainty for the total drag forces in [N]

Turbulence model	Fine Grid#1 Forces [N]	Medium Grid#2 Forces [N]	Coarse Grid#3 Forces [N]	Discretization error δG [%]	Discretization uncertainty UG [%]
SA	7.7207665	7.6112397	9.1473354	**0.1089**	**0.1361**
KES	10.274434	10.302896	10.290131	0.2253	0.2816
KERNG	6.1109277	6.2389111	6.488291	2.2080	2.7600
KER	6.5435718	6.6625013	6.8730493	2.3593	2.9491
KWS	32.414518	44.709143	45.449136	2.4291	7.2873
KWSST	11.73214	12.868474	8.0203764	2.9652	3.7065
RSM-LR	9.5472548	9.1122949	16.079741	0.3033	0.3792
RSM-LPS	Divergent	Divergent	Divergent	-	-
RSM-QPS	Divergent	Divergent	Divergent	-	-

3.2.3. Conclusion

After applying ASME Validation and Verification procedure [17], it is found that the turbulence model Spalart-Allmaras (abbreviated SA) available on FLUENT yields 0.l1 % of discretization error which is less than others. So, Spalart-Allmaras model is the suitable turbulence model for simulating viscous incompressible flow around ROV body in this study. Therefore, Spalart-Allmaras model will be use to perform simulation in order to investigate the propulsive performances of the ellipsoidal ROV.

3.3. Validation

In order to validate numerical computations some assumptions are needed:

- Numerical uncertainty from the bare hull is equal to the one of the ROV with channels; bare hull and ROV body have same shape and dimensions, moreover it is complicated to generate three significant meshes on channels.
- Simulation results error δ_{SIn} due to simulation input parameters and its associated uncertainty U_{SIn} are neglected; the input data and parameters i.e. water density and viscosity, are set as the nominal value or assumed as null.

3.3.1. Experimental uncertainty

The experimental resistance tests of the studied ROV have been performed in forward motion by **Obreja and Domnisoru [4].** The experimental tests were performed at 20°C temperature water in the towing tank of the Faculty of Naval Architecture of the “Dunarea de Jos” University of Galati (figure 3.2).

Built by the British Company Cussons Technology, the towing tank has 45*4*3 meters in size and is able to tow experimental models at a maximum speed of 4 m/s thanks to one fitted automatic carriage.

Figure 3.9: The towing tank of the “Dunarea de Jos” University of Galati, Naval Architecture Faculty.

The ROV was built at a 1:1 scale and was coupled to the carriage thanks to one hydrodynamic profile in order to be submerged.

V= 1 m/s V=1.5 m/s

Figure 3.10: ROV-hydrodynamic support system [**4]**

According to **Obreja and Domnisoru [4],** the measurement error of the forward motion resistance tests was about 2%. Therefore, the experimental uncertainty U_D will be considered as 2%.

3.3.2. Validation uncertainty

Taking in account the assumptions made in *section 3.3*, the validation uncertainty U_{VAL} is reduced to:

$$U_{VAL}^2 = U_{SN}^2 + U_D^2 \tag{3.22}$$

As mentioned above, experimental uncertainty is equal to 2% and knowing the numerical uncertainty which is 0.l4 % (*see table 3.2*), the validation uncertainty can be deduced. So, the validation uncertainty U_{VAL} for simulating flow around ROV body will be 2%.

$$\boldsymbol{U_{VAL} = 2\%.}$$

The validation comparison error E for the nominal speed has been computed as difference between CFD and EFD results for the service speed of 3 knots and is equal to 0.82%. According to paragraph 3.1.1, $|E| = 0.82\%$ is less than $U_{VAL} = 2\%$. This means that the modeling error $\boldsymbol{\delta_{SM}\epsilon}[-1.18; 2.82]$ is smaller than the noise originated by the numerical, experimental and input parameters uncertainty.

4. SIMULATION OF THE FLOW AROUND A FULLY SUBMERGED REMOTELY OPERATED VEHICLE (ROV)

The aim of the study is to investigate the propulsive performance of the moving ROV described in *figure 1.8* (*section 1.4).* The study of the ROV resistance problem is necessary for understanding propeller influences. Simulations will be focused on the longitudinal displacement of the ROV because that is its main working axis.

In order to determine and investigate on the resistance, numerical simulation of the turbulent flow around the ROV body is performed at five speeds of interest ranging from 1 m/s to 2 m/s in freshwater conditions according to FLUENT ($\rho = 998.2\frac{kg}{m^3}, \mu = 1.003 * 10^{-3}$Pa . s), similar to the experimental conditions, *section 3.3.1*.

Two cases were considered:

- Simulation around the ROV without propellers called “ROV’s hull” in order to determine the resistance of the ROV body.
- Simulation around the ROV with propellers called “ROV body”.

Both cases have same simulating condition and grid generation; the difference is only about their geometry. In other word “ROV’s hull” is the “ROV body” without propellers.

Figure 4.1 shows the computational domain which is the same used for the simulation of the bare hull seen in *subsection 3.2.1.1*.

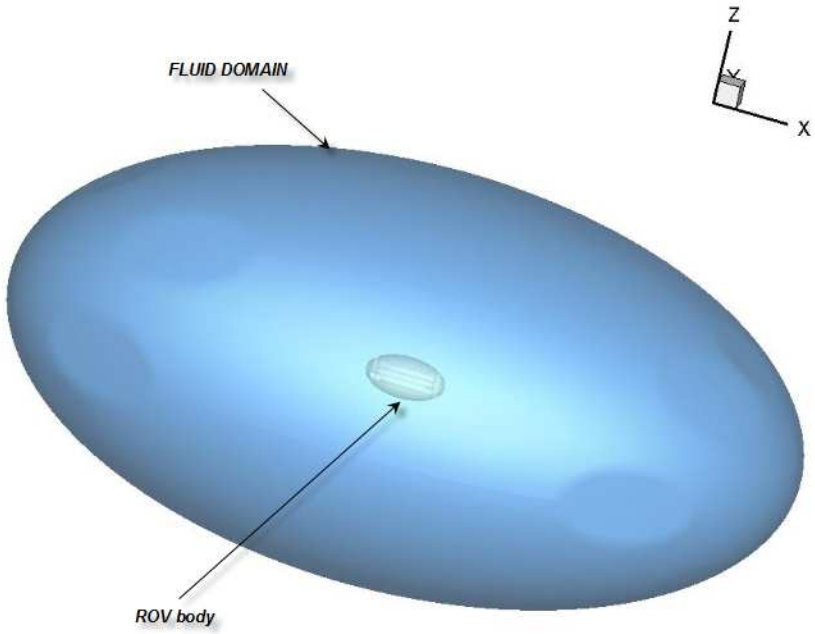

Figure 4.1: Perspective view of the computational domain, ROV body

4.1. Grid Generation

Structured and unstructured grids are modeled for theses simulations. The mesh generation was the same performed for bare hull case (*in section 3.2.1.2*), except the mesh created on cylindrical channels and actuator disk area considered as propeller surface. A structured hexahedral mesh is employed inside the fluid domain.

The figures below depict grids on and around the ROV body.

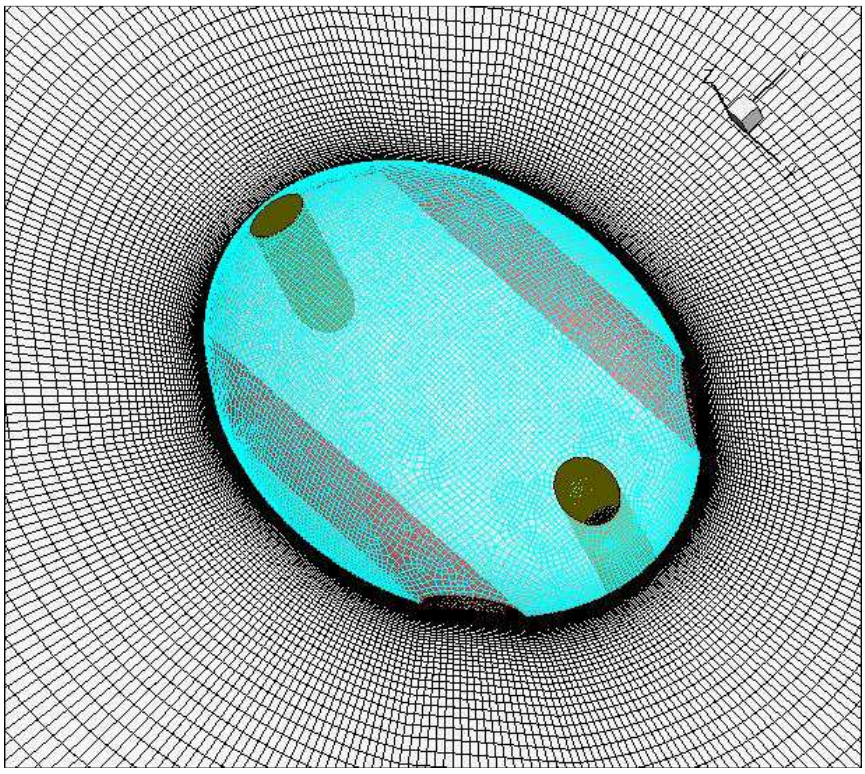

Figure 4.2: Mesh around ROV body

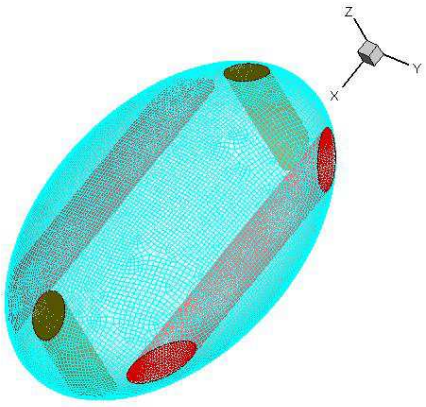

Figure 4.3: Grid on the ROV body

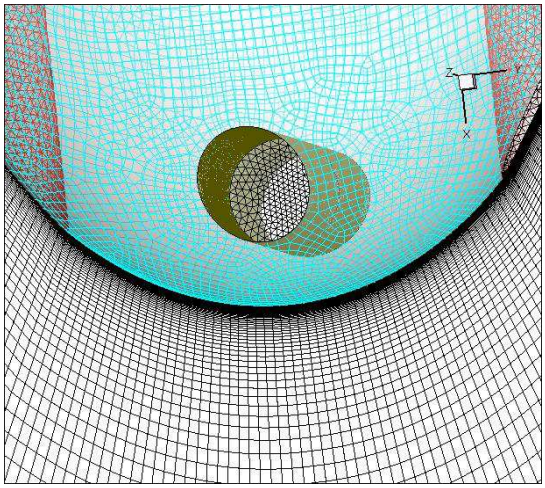

Figure 4.4: Boundary layer meshing

As defined in the scope of work, the ROV has four actuator disks mounted into two cylindrical channels parallel with x-axis corresponding to the main axis of the ellipsoidal ROV and the other two in channels parallel with z-axis.

Tetrahedral volume mesh is generated on each cylinder volume. Therefore triangular surface mesh is created on actuator disk area.

The following figures show the mesh generated on these important parts of the ROV

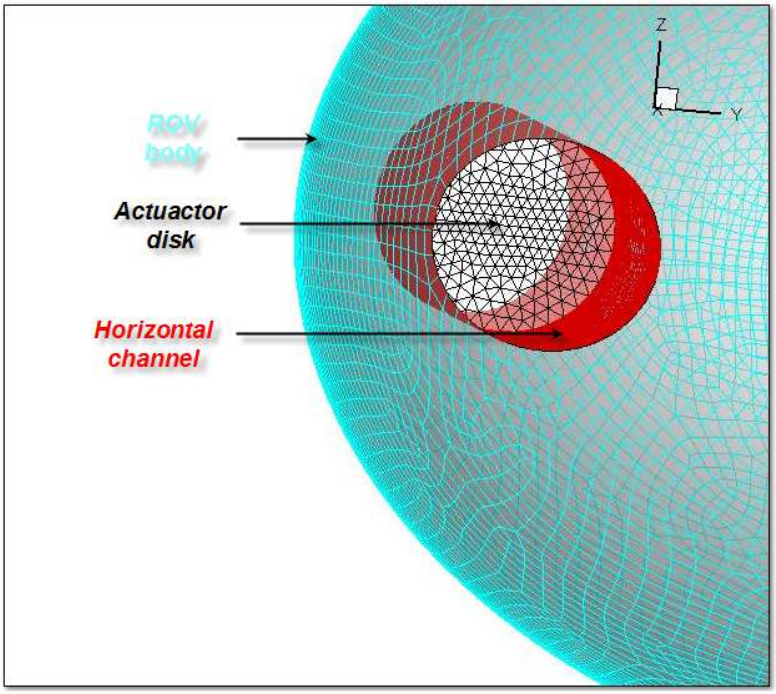

Figure 4.5: Grid on propulsive system of the ROV

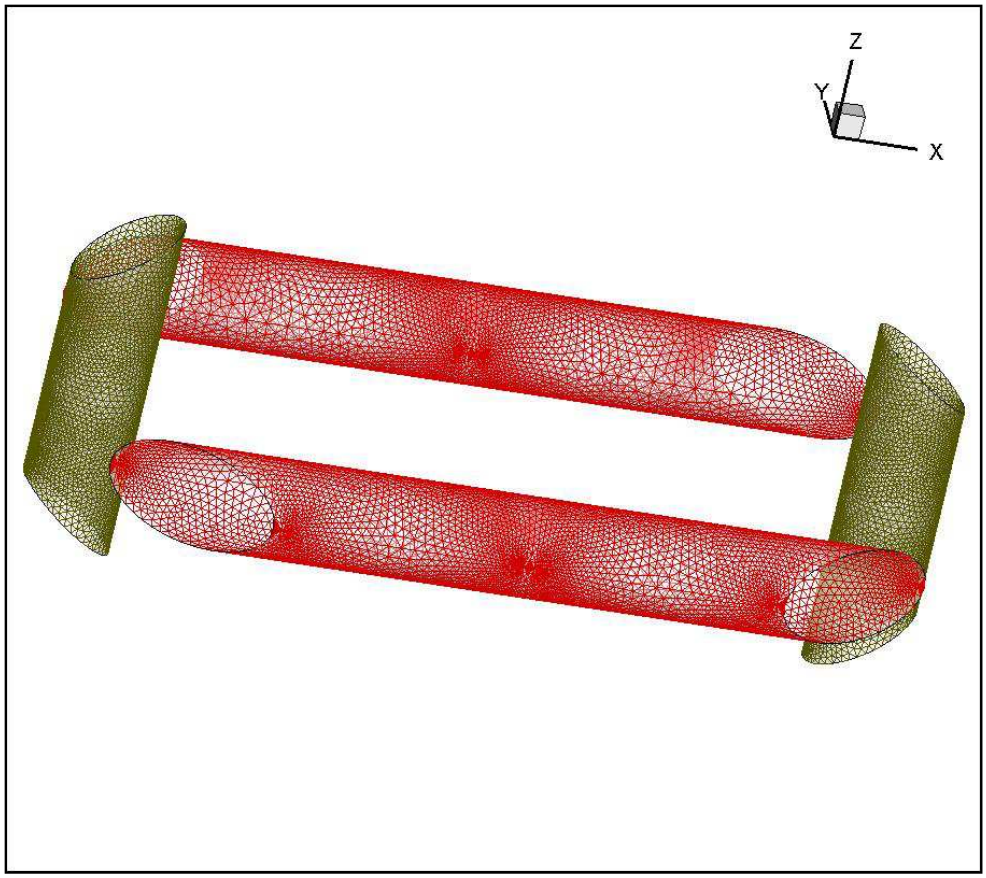

Figure 4.6: Grid on channels

4.2. Boundary and initial conditions

4.2.1. ROV body case

Velocity Inlet conditions are imposed on the far field domains, while outflow condition was imposed at the exit of the ROV's hull. No-slip boundary condition is chosen for the ROV surface and also for horizontal and vertical channels. Fan boundary condition is used for the actuator disk surface in which the pressure jump is introduced according to the corresponding velocity.

The turbulent length scale is equal to 0.035 m, meaning 7% of the ROV's length and the turbulent intensity set up to 3%.

Figures below describe boundaries conditions.

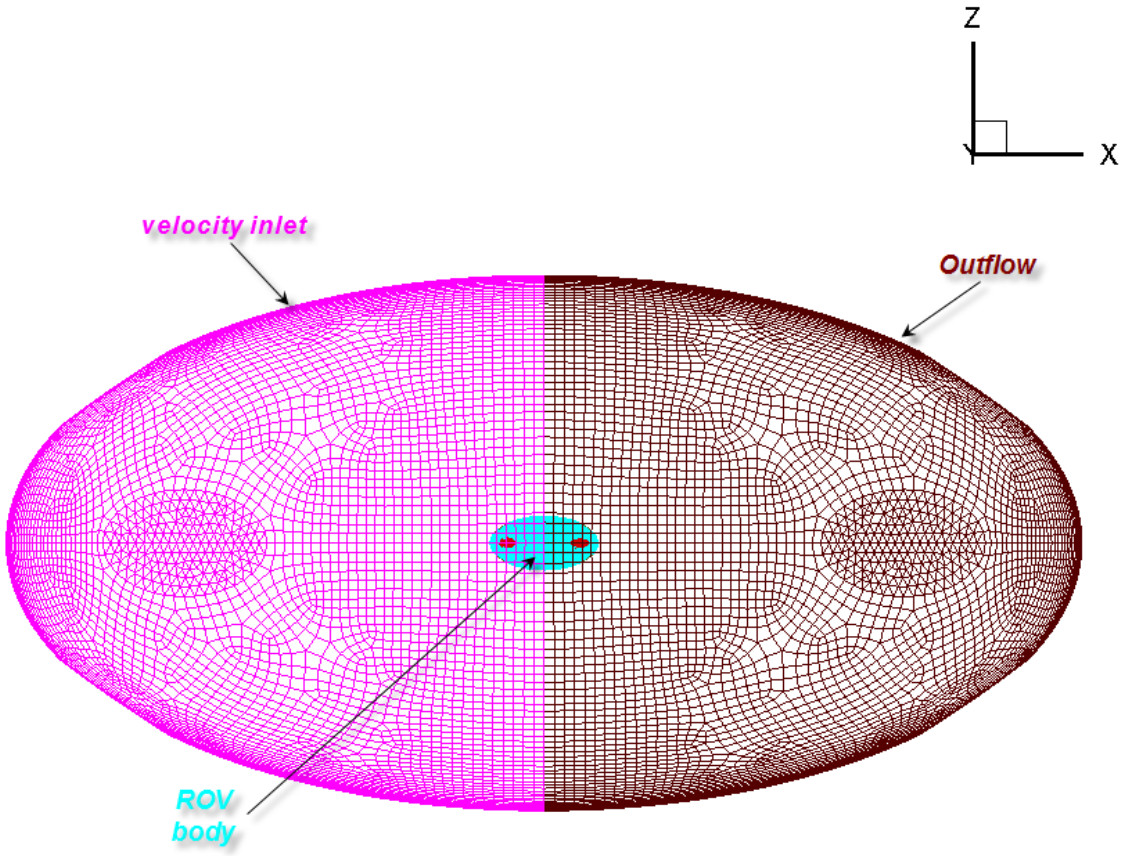

Figure 4.7: Boundaries conditions concerning the domain

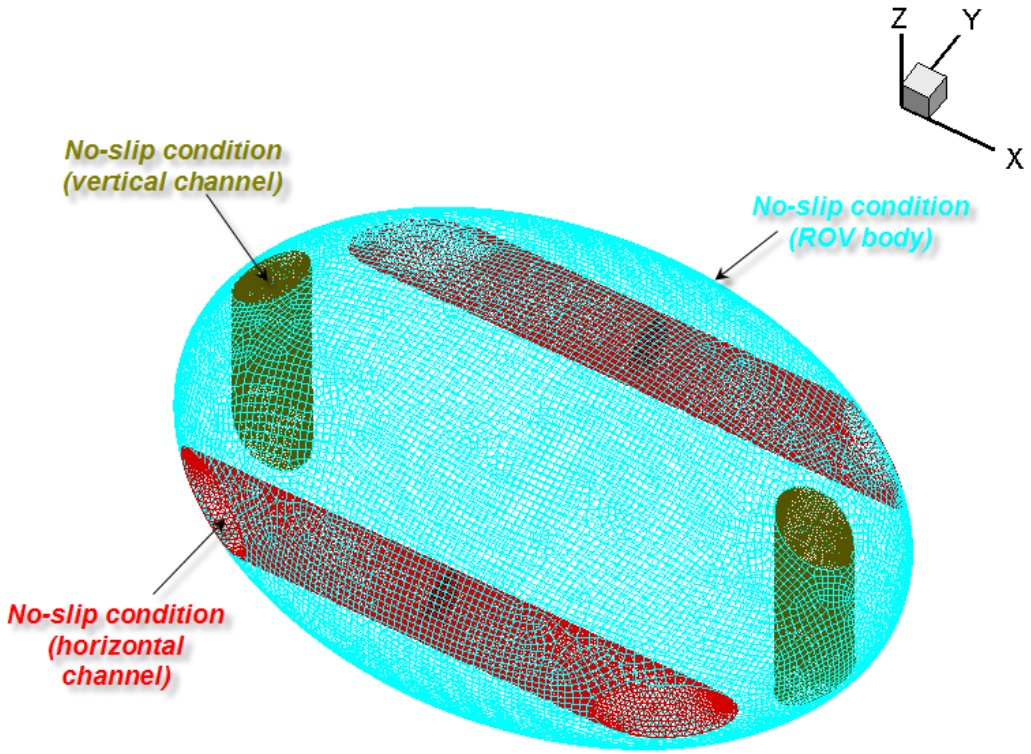

Figure 4.8: Boundaries conditions concerning the entire ROV

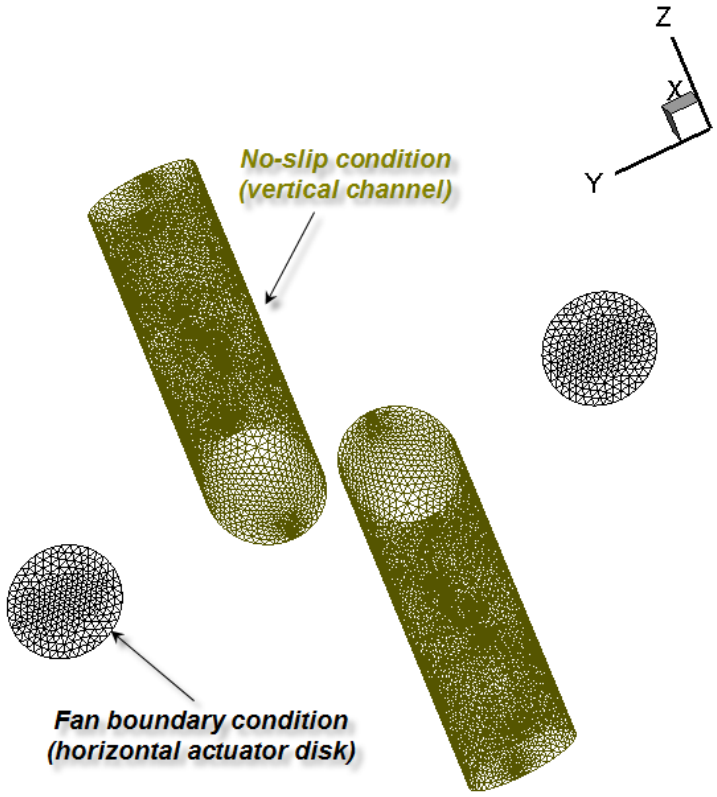

Figure 4.9: Boundaries condition concerning the propulsion system, ROV body case

4.2.2. ROV's hull case

The boundary and initial conditions are also the same used for the ROV body case mentioned above except for the fan boundary condition which has been removed. So, the actuator disk surface is defined as interior boundary condition in order to obtain the hull resistance of the ROV without the effect of propeller modeled as actuator disc.

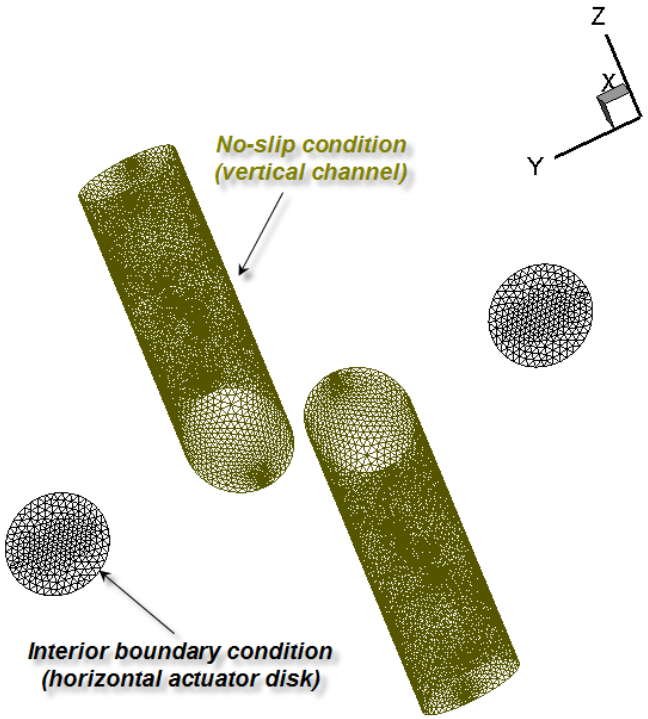

Figure 4.10: Boundaries conditions concerning the propulsion system, ROV's hull case.

4.3. Solver setup

The solver and the used numerical schemes are the same employed for the case of the bare hull seen in *section 3.3.1.4.* The numerical simulations were performed at the angle of attack equals to zero and the reference values used for computing total drag forces are reported below:

- Area $A = 1m^2$
- Density $\rho = 998.2\ kg/m^3$
- Pressure $p = 0$ Pa
- Length $L = 1\ m$

Cause of the flow symmetry in both XY-plane and XZ-plane, the mean lift and moment coefficient are zero.

5. RESULTS AND DISCUSSIONS

Simulations have been performed at velocity ranging from 1m/s to 2 m/s around the "bare hull," "ROV's hull" and the "ROV body".

"Bare hull," "ROV's hull" and the "ROV body" are different configurations made in *section 1.4* in order to study the selected ROV which has been described in *subsection 1.3.1*.

5.1. ROV resistance

5.1.1. Numerical results from ROV's hull case

The purpose of this simulation is to analyze the flow around the "ROV's hull" in order to obtain through this analysis the resistance and effective power of the studied ROV defined *in section 1.3.1*. It will allow one investigation on the propulsive performance of this vehicle a little later.

The total drag forces acting on the ROV is determined by simulating the flow around the "ROV's hull".

The results of this simulation are presented in Table 5.1, together with the statistical results and the experimental data from **Obreja and Domnisoru [4],** for all five speeds of interest.

Table 5.1: Resistance of the ellipsoidal ROV

Speed, v [m/s]	**1**	**1.25**	**1.5432**	**1.75**	**2**
Reynolds number	4.98E+05	6.22E+05	7.68E+05	8.71E+05	9.95E+05
Statistic Method [N]	9.79	12.97	15.95	18.56	20.68
EFD [N]	5.7	8.83	13.42	17.18	20.89
CFD [N]	5.77	8.94	13.53	17.33	22.54
Validation comparison error $\boldsymbol{E = \frac{(CFD-EFD)}{EFD} * 100}$[%]	1.23	1.25	0.83	0.87	7.89

It can read from the table above the resistance of the ROV computed numerically at the service speed (1.5432 m/s).

The error is less than 2% for the speeds of 1 m/s and 1.25 m/s; And also less than 1% for the speeds of 1.5432 m/s and 1.75 m/s.

The results of the turbulent flow simulation around the “ROV’s hull” has been also plotted for each speed of interest. The following figure presents the total drag forces computed numerically, and the statistic and experimental ones. It can be observed that the ROV increases in resistance when the speed is raised.

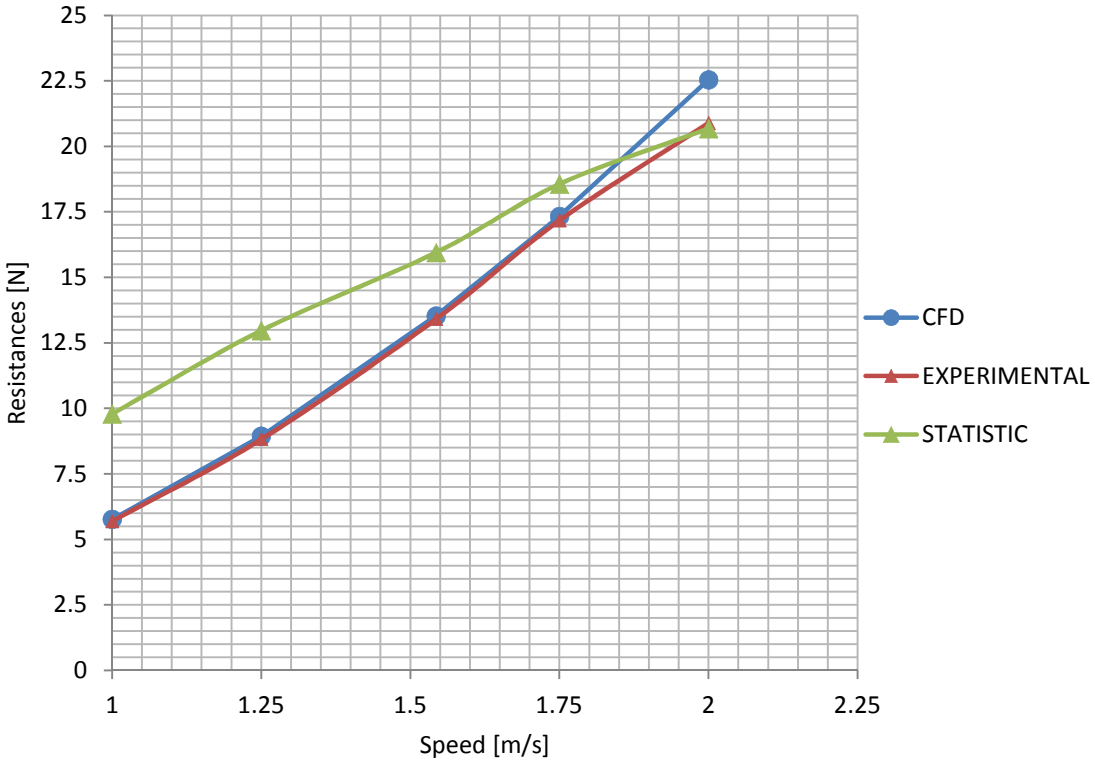

Figure 5.1: Comparison between CFD and EFD results.

For the last speed, CFD and experimental results are bit different with an error of 8%, but resistance versus speed curves slope are almost the same.

It can observe that on the regime of working of the ROV the error is less than 2%.

In conclusion simulation results have good agreement with the experiment data.

The effective power corresponding to the resistances is plotted below as function of speed.

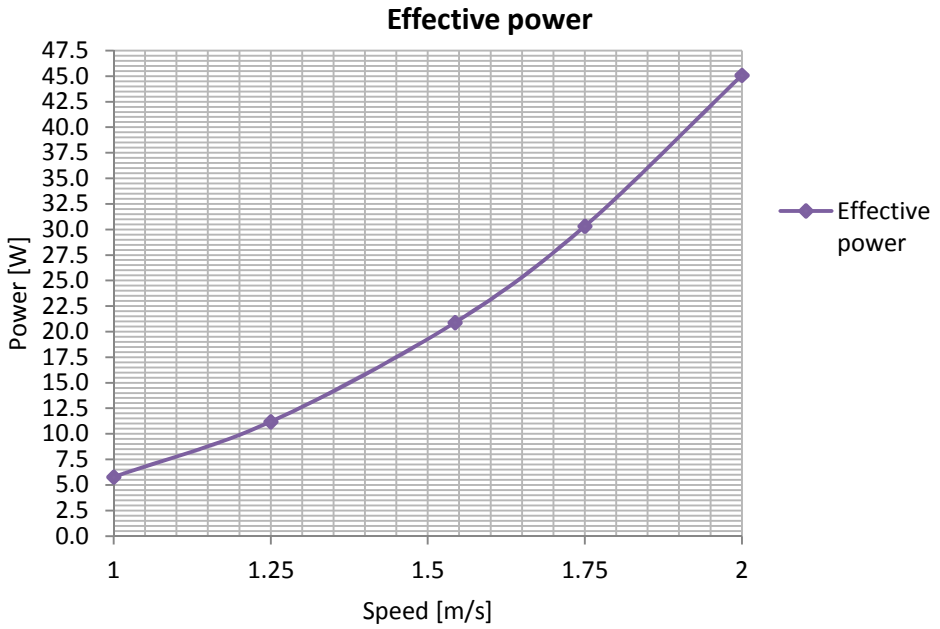

Figure 5.2: ROV effective power versus speed

5.1.2. Axial velocity distribution

5.1.2.1. Bare hull case for all speeds

The following figure presents the distribution of the axial velocity behind the bare hull.

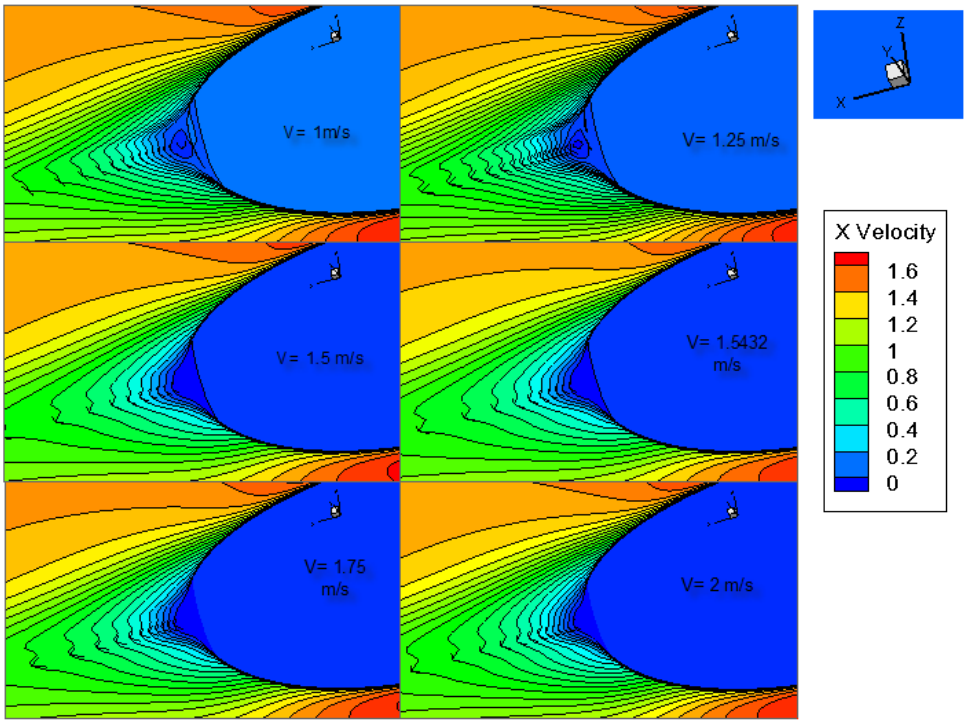

Figure 5.3 : Axial velocity distribution behind the bare hull

It can be noticed that the velocity behind the bare hull is equal to zero. This is due to the effect of the vortices formed during the fluid motion. Vortices are reduced when the velocity is increasing.

5.1.2.2. ROV's hull case for service speed

This figure 5.4 shows the distribution of the axial velocity around the ROV without propeller.

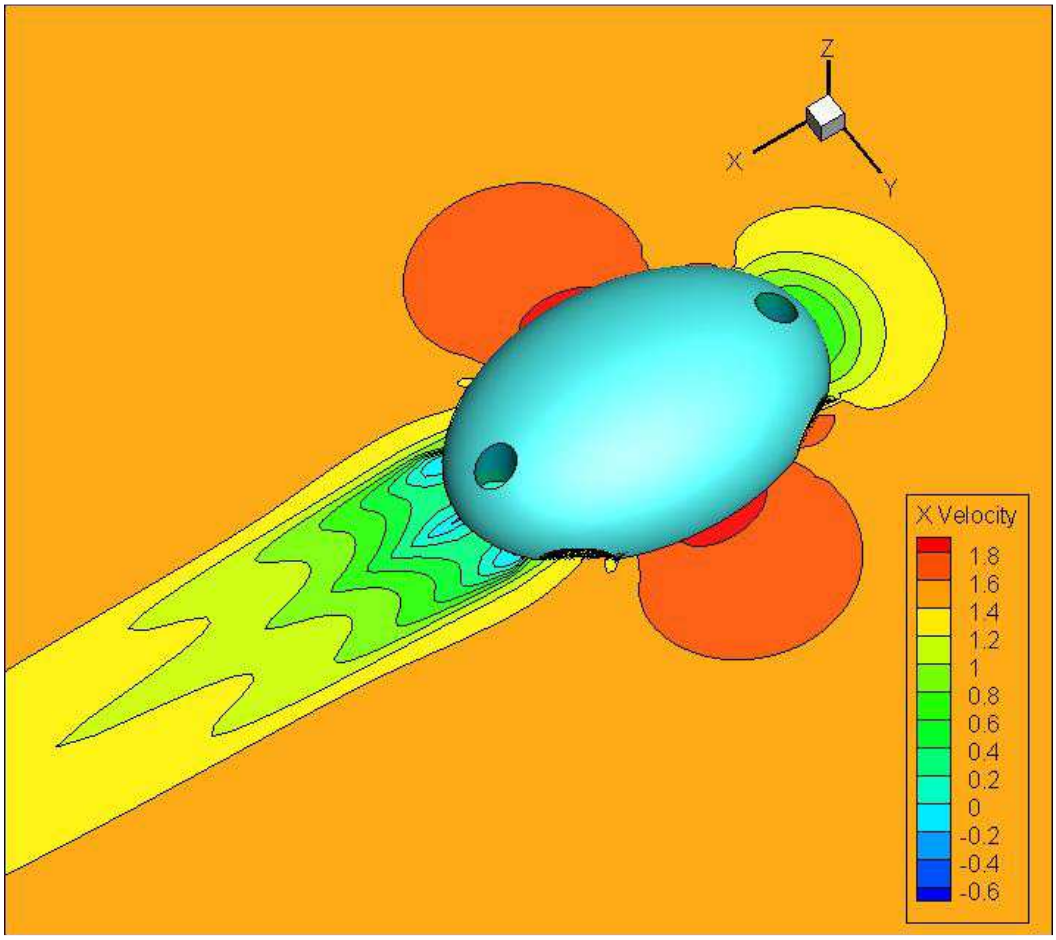

Figure 5.4: Axial velocity distribution for the service speed of 1.5432 m/s

The velocity is greater at the middle of the body and negative behind the ROV body. This negative value of the velocity indicates the creation of the vortices behind the ROV.

In order to provide the details of flow development over the ROV length, streamlines pattern are plotted in figure 5.5 and also in figure 5.6. Streamlines are suitable to study the nature of fluid motion in the complex flow field.

The streamlines are symmetrical in respect to the flow axis and it can be observed turbulent flow separation point in figure 5.6 leading to the generation of the vorticity region or separated region.

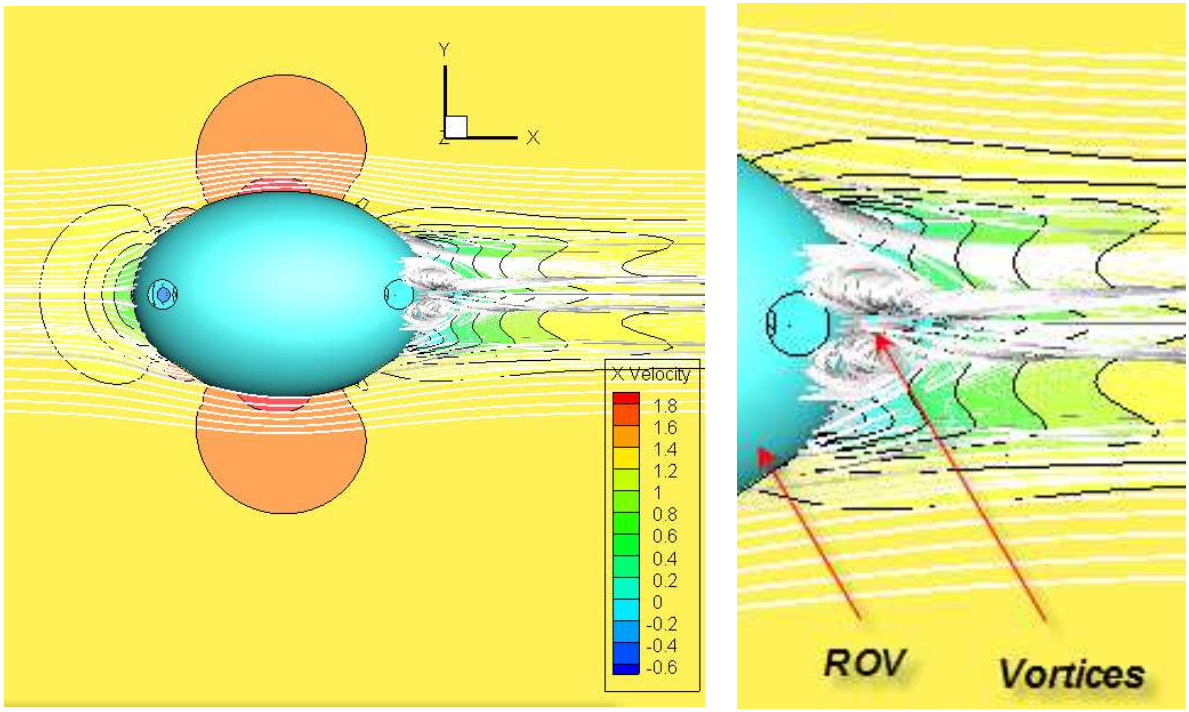

Figure 5.5: Streamlines and vortices around the ROV for service speed

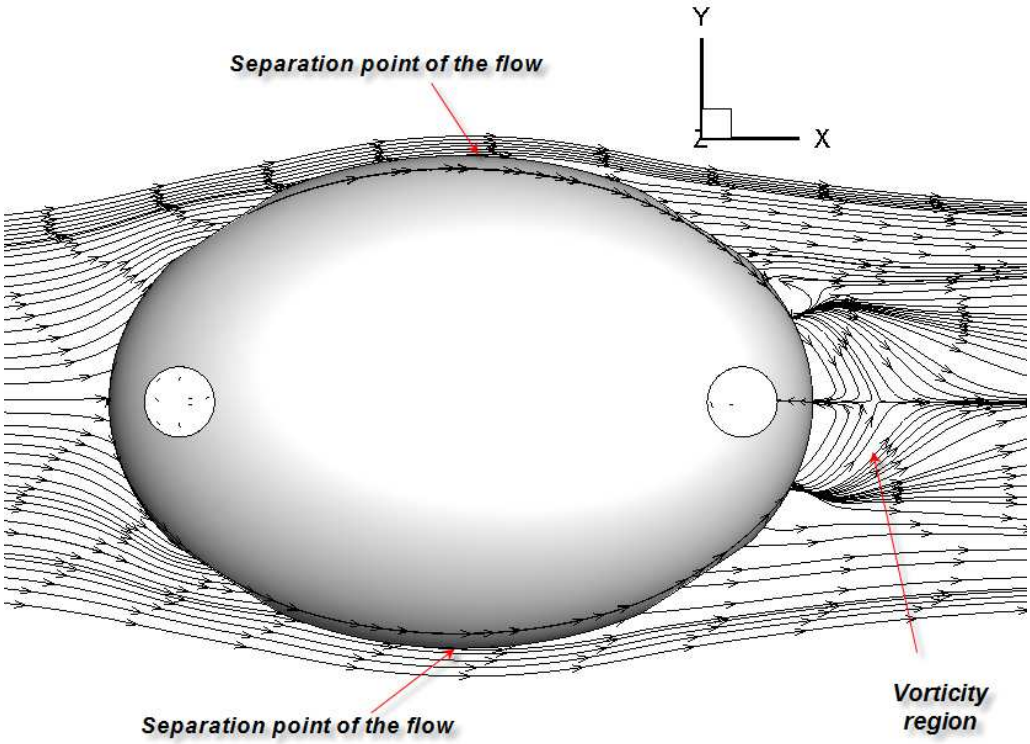

Figure 5.6: Vorticity region, ROV's hull case

5.1.3. Pressure distribution

5.1.3.1. ROV's hull case for service speed

Figure 5.7 depicts the pressure distribution around the ROV without propeller at service speed.

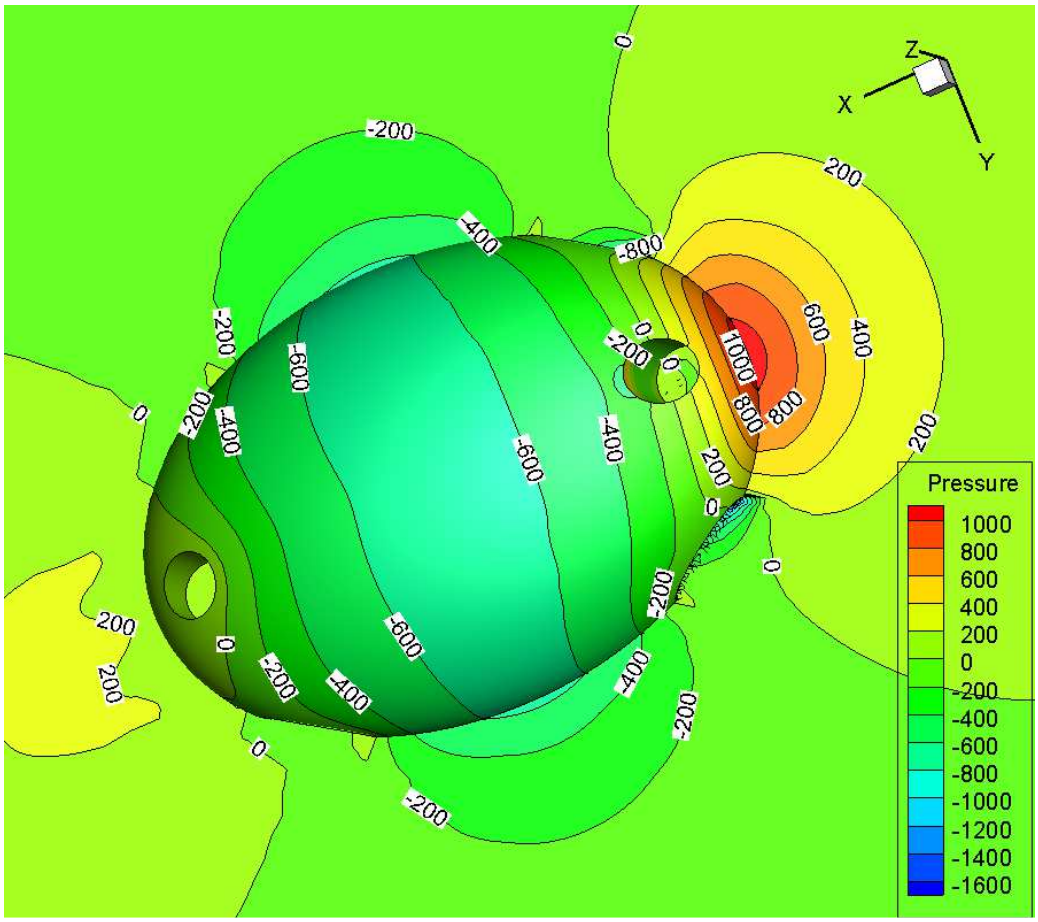

Figure 5.7: Pressure distribution for the service speed

It can be observed one variation of pressure along the length of the ROV at the service speed. The pressure is high in front the ROV and falls to zero behind the ROV body.

5.1.4. Comparison between all cases

Simulations have been performed at velocity ranging from 1m/s to 2 m/s around all bodies or all configurations as mentioned at the beginning of this chapter.

Figure 5.8 shows a comparison between the drag forces computed on the three configurations considered in *section 1.4*.

For all configurations, the total drag force increases with the speed. The ROV's hull case provides large drag forces than bare hull case. This is due to the importance of the wetted area inside channels. On the other side the ROV's hull case gives less drag forces the ROV body

case. This second situation is results of the effect of the actuator disk leading to more significant viscous component of the resistance.

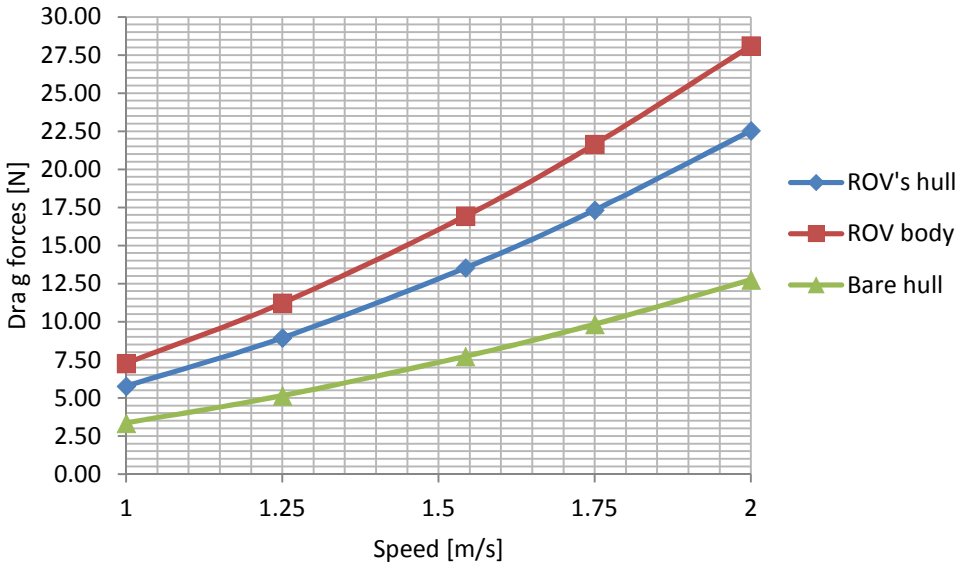

Figure 5.8: Comparison between all cases

5.1.4.1. Velocity distribution for design speed

In order to compare velocity distribution, simulations were carried out around all bodies or configurations at the same service speed of 3 knots. The simulation condition was the same mentioned in chapter four.

Figure 5.9 describes the velocity distribution around the “bare hull”, the “ROV’s hull” and the “ROV body”.

For the bare hull case it was shown that the velocity relative to the upstream is reduced behind the bare hull with small disturbance due to the vortices. However, in the ROV’s hull case the disturbance is increased behind the body. This is due to the acceleration of the flow from the cylindrical channels. The last case “ROV’s body” is quite different to the others cause of the consideration of the active disk considered as propellers. The flow is accelerated behind the body by the actuator disk limiting the development of the vortices. The vortices region behind the ROV is known as separated region due to the flow separation.

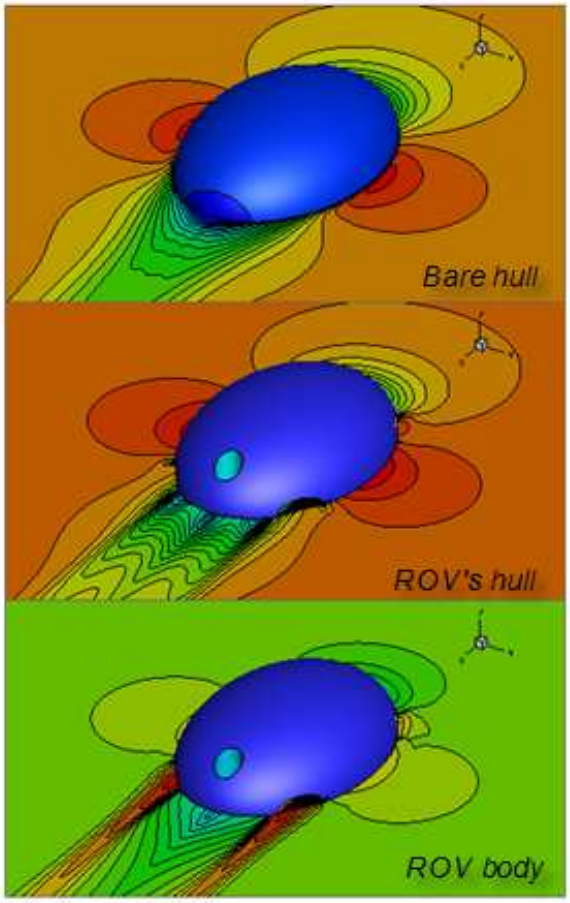

Figure 5.9: Comparison of the axial velocity for design speed, all cases

5.2. Propeller effect

After computing the resistance of the ROV without propeller in *section 5.1.1*, attention will be put on the effect of the propellers by simulating turbulent flow around the "ROV body" which is the ROV with propeller. For that, propellers have been reduced to actuator disc in order to generate thrust in the flow. Knowing the total resistance required to tow the ROV, the computation of the pressure jump necessary to set up on each horizontal actuator disc cause of the main working regime of the ROV which is the longitudinal displacement (along x-axis). Propellers are working in pair on each direction considered.

Numerical computations are also performed for the same speeds of interest in order to obtain the total drag forces (representing the thrust) which are the main variables of these simulations.

The angle of attack is equal to zero; the mean lift and moment coefficient are should be zero because the flow is symmetrical in both XY-plane and XZ-plane.

The result of the simulation around the “ROV body” is given by the table 5.3 in the yellow column. The difference of drag forces between “ROV’s hull” case and “ROV body” yields the influence of propellers or the propellers effect on the ROV resistance.

The resistance R_T from the “ROV’s hull” case is total resistance of the ROV body and the resistance T from the “ROV body” is the thrust.

Table 5.3: Drag forces computed from ROV with Propellers

Velocity **[m/s]**	**“ROV’s hull” Drag force** **[N]**	**Section Area of the disk** **[m2]**	**Total Pressure jump** **[Pa]**	**Pressure jump per Propeller** **[Pa]**	**“ROV body” Drag force** **[N]**
1	5.77	0.001963	3629.01	1815	7.26
1.25	8.94	0.001963	5623.582	2812	11.22
1.5432	13.53	0.001963	8508.915	4254	16.93
1.75	17.33	0.001963	10894.57	5447	21.65
2	22.53	0.001963	14171.68	7086	28.11

The figure below presents the influence of the horizontal propellers on resistance

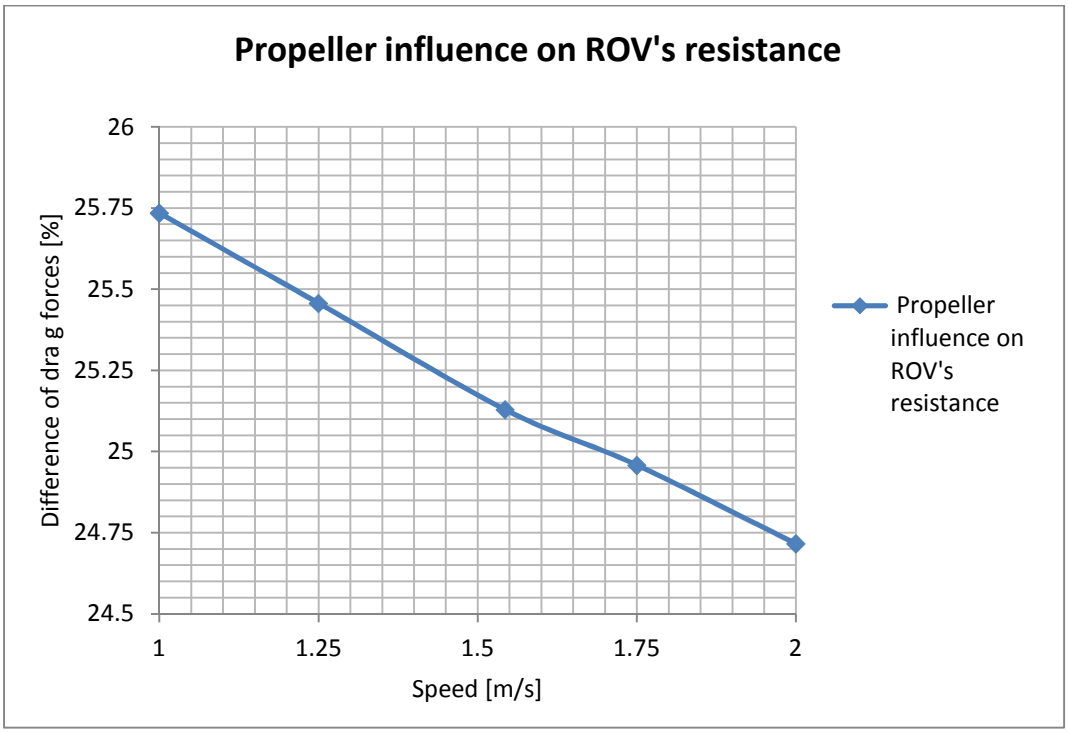

Figure 5.10: Effect of horizontal propellers

Quite smaller, the difference of drag forces percentage decreases when the speed is increased. At high velocity, the ROV produces less resistances, then less energy consumption if the concerning velocity doesn't generate vibration.
The values of the thrust and the thrust deduction fraction are given in table 5.4.

Table 5.4: Thrust and thrust deduction fraction computation.

Velocity [m/s]	**Thrust per propeller [N]**	**Thrust deduction fraction, t**
1	3.62850495	0.20467359
1.25	5.610372	0.20291204
1.5432	8.4667535	0.20082444
1.75	10.825771	0.19973099
2	14.0549425	0.19817943

The table above shows that for increasing the velocity the force developed by the ROV propellers increases and the thrust deduction fraction decreases.

5.2.1. Axial velocity distribution

The distribution of the velocity around the ROV and also inside the cylindrical channels can be observed in figure 5.11. Also the turbulent separation point can be identified in Figure 5.12.

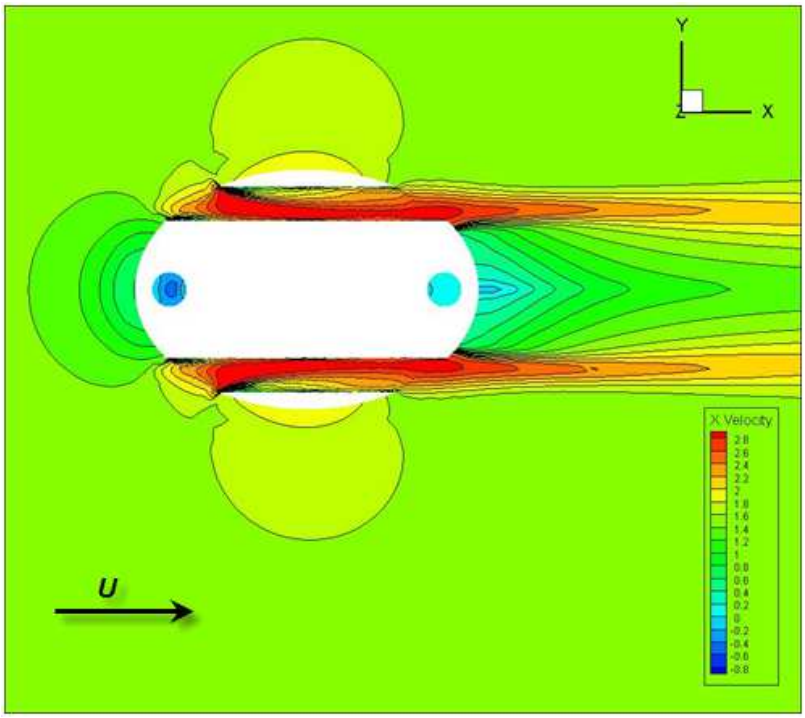

Figure 5.11: Distribution of the velocity at service speed, ROV body case

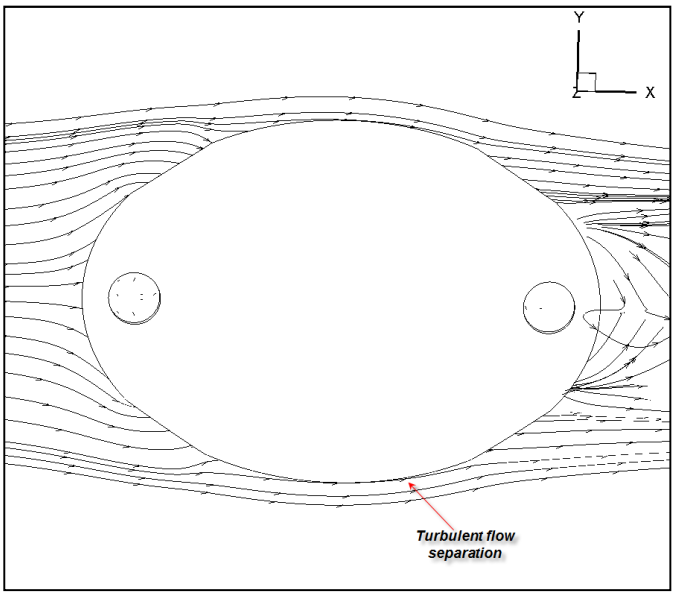

Figure 5.12: Turbulent flow separation at V= 1.5432 m/s, ROV body case

The following figures below depict the distribution of the axial velocity around the ROV body for different speeds ranging from 1 m/s to 2 m/s.

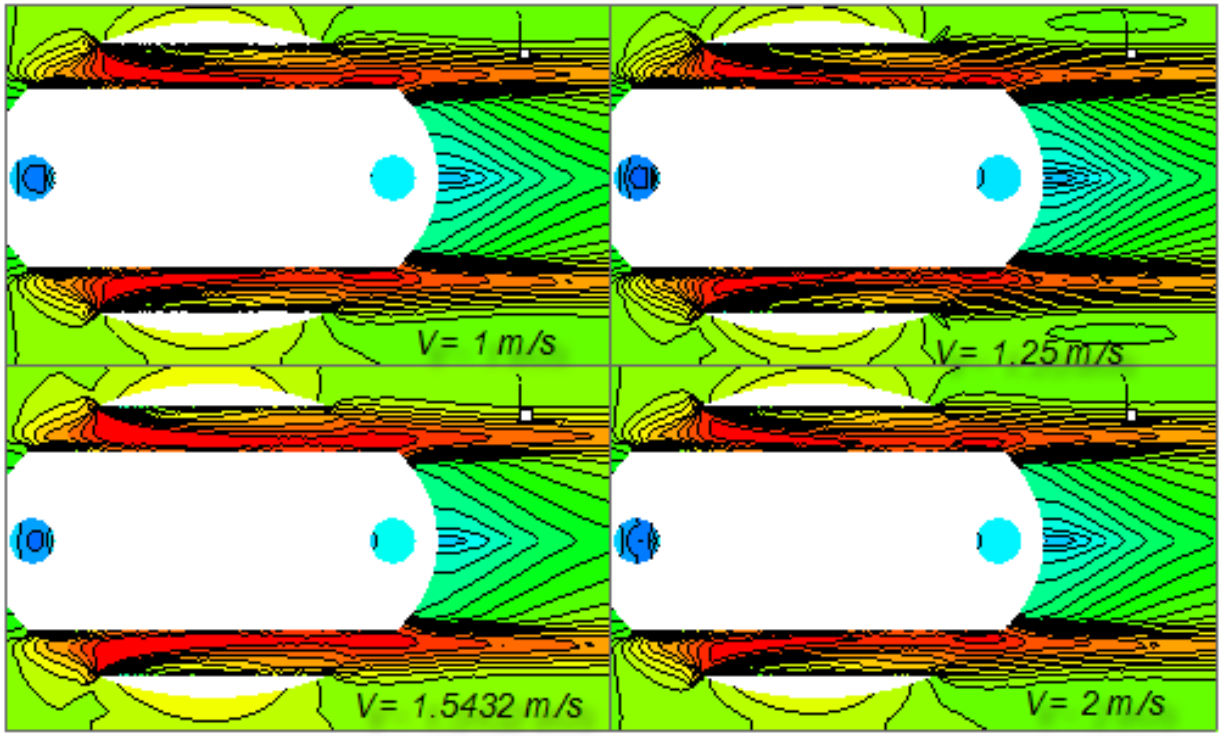

Figure 5.13: Comparison of the velocity distribution, ROV body case

The velocity is greater in the channels; this is due to the action of the actuator disc representing propellers. From 1 m/s to 2 m/s the vorticity is reduced by the action of the propellers which accelerate the flow behind the ROV and also the separation point is affected.

5.3. Flow separation comparison between ROV's hull" and the "ROV body" cases

After simulating turbulent flow around the "ROV's hull" and also around the "ROV body", it was identified on Figure 5.14 and Figure 5.15, where the fluid particle was detached from the ellipsoid surface.

These figures show the location of the turbulent flow separation point at nominal velocity.

It is known that the location of the separation point depends on the surface roughness, the Reynolds number like the case above. But, the presented cases tend to focus on the presence or not of propellers as variant.

In order to reduce the energy consumption, it is better to keep the local flow attached for as long as possible.

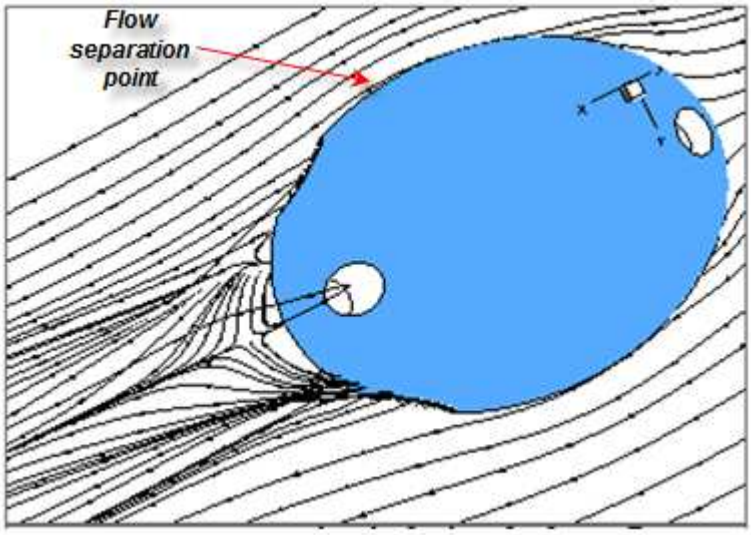

Figure 5.14: Turbulent flow separation at V= 1.5432 m/s, ROV's hull case

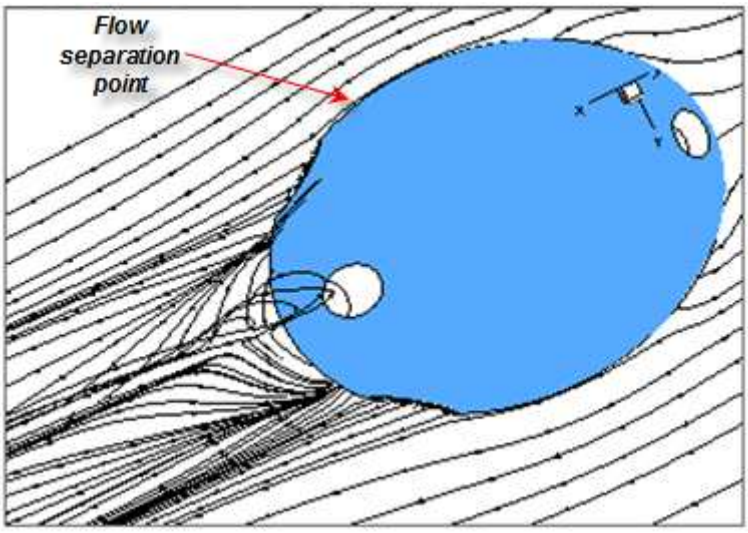

Figure 5.15: Turbulent flow separation at V= 1.5432 m/s, ROV body case

It can be noticed that the ROV body case keep the local flow attached more than the ROV's hull case. The effect of the flow separation is observed by means of decreasing velocity far downstream. The separated region behind the ROV justifies the reattachment of two flow streams.

5.4. Angle of attack

The angle of attack is the angle between the reference line on the ROV and the vector representing the relative motion between the ROV and the oncoming flow. In order to investigate on its effect on the ROV body, simulations were performed at various angles of attack ranging from 0° to 30° for the service speed. The solver setup was kept the same as ROV body case in chapter four. The ROV body was reported to a Cartesian system of coordinates having the x-axis horizontal according to the center line of the ROV, the y-axis oriented laterally and the z-axis is vertical. The effect of the angle of attack will be study in both XY-plane and XZ-plane.

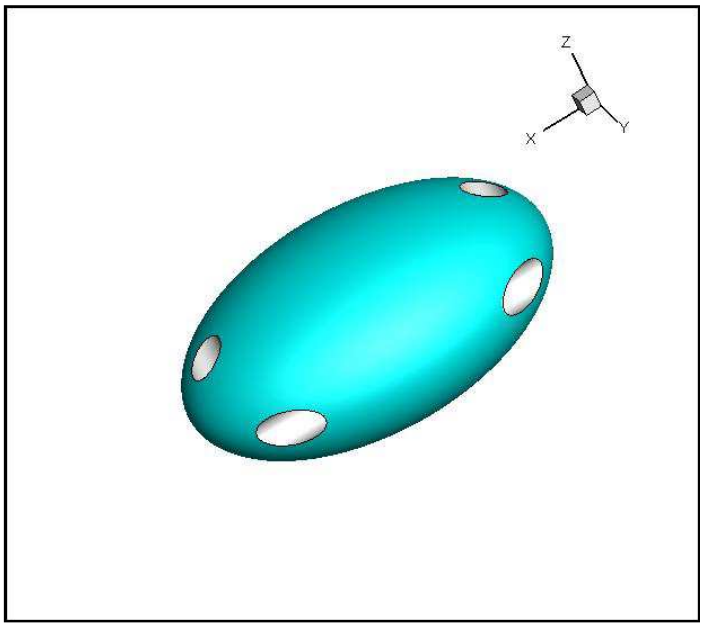

Figure 5.16: ROV reported to a Cartesian system of coordinates

5.4.1. Force coefficients

5.4.1.1. Force coefficients in xy-plane

The main parameter which depends of the angle of attack is the force coefficients.

In figure 5.17 are plotted the total drag force coefficient, the lateral force coefficient and the lift force coefficient as a function of angle of attack ranging from 0° to 30° in xy-plane.

The lift coefficient has negative value near to zero. This coefficient can be neglected in xy-plane.

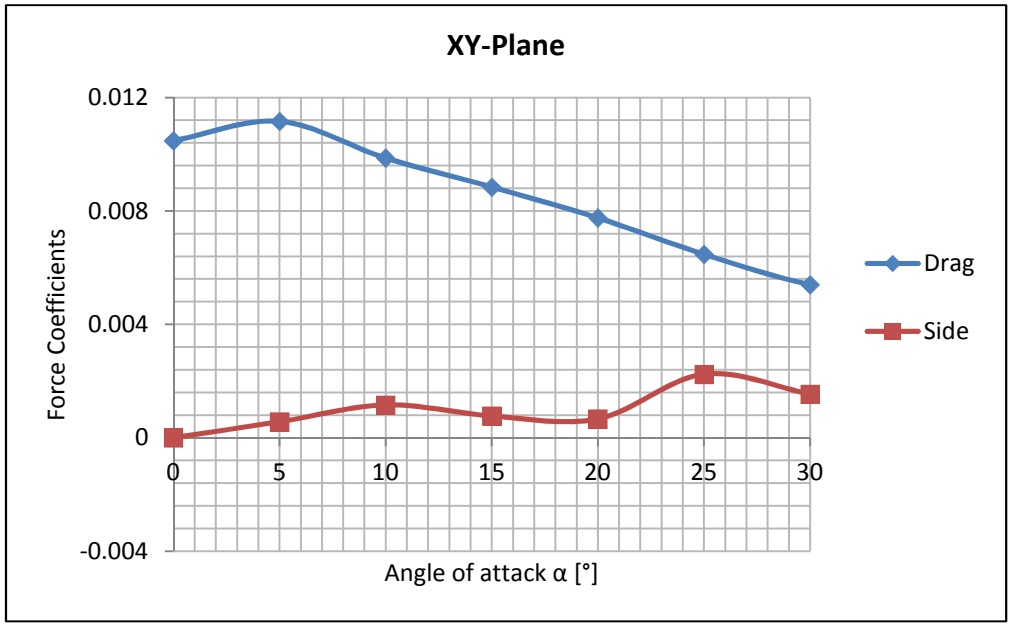

Figure 5.17: Force coefficients acting on the ROV body in XY-plane

The total drag coefficient is maximal at $\alpha = 5°$ and starts to decrease from this angle. This decrease is linear from $\alpha = 10°$.

It can be noticed that the lateral force coefficient is smaller than the drag coefficient at each angle.

Figure 5.18 shows the evolution of moment coefficient at different angles of attack.

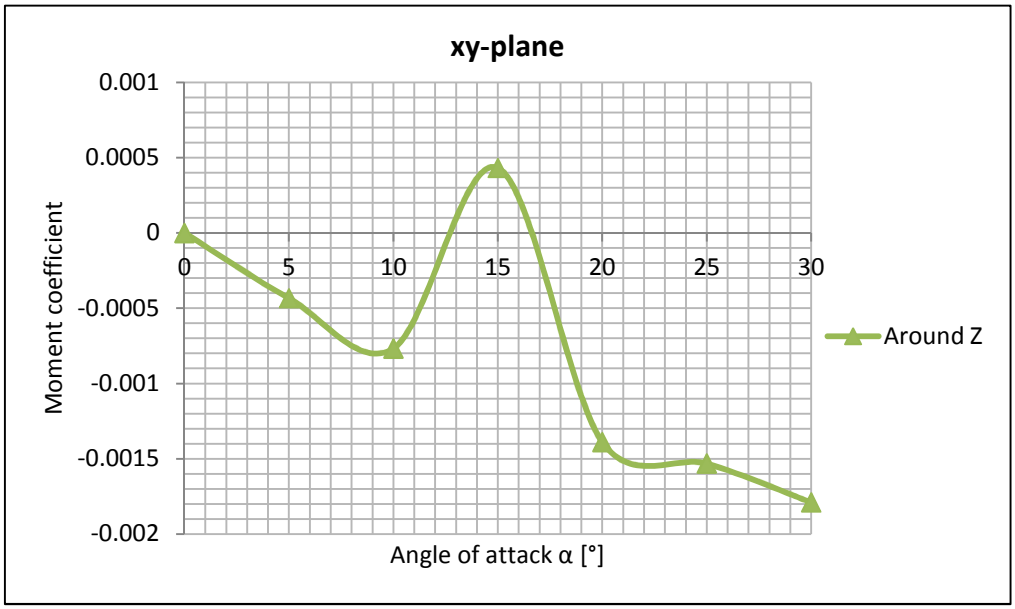

Figure 5.18: Moment coefficient acting on the ROV body in XY-plane

In xy-plane, the maximum moment is reached around z-axis at $\alpha = 15°$ and the drag force is more significant than others forces.

5.4.1.2. Force coefficients in xz-plane

Figure 5.19 shows the drag coefficient, the lift coefficient and the lateral force coefficients as a function of angle of attack in xz-plan. Also the moment coefficients are plotted in figure 5.20.

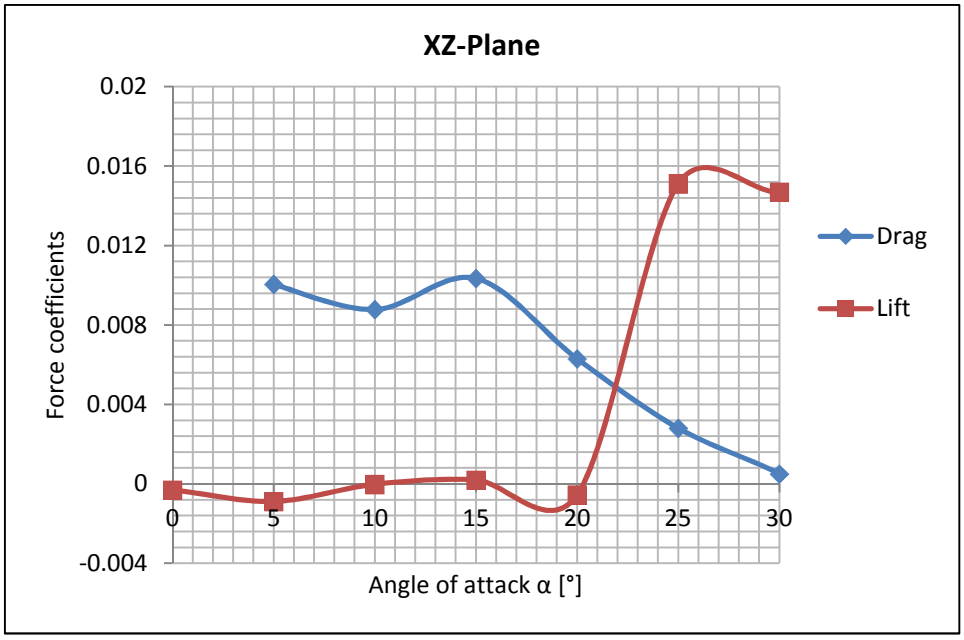

Figure 5.19: Force coefficients acting on the ROV body in XZ-plane

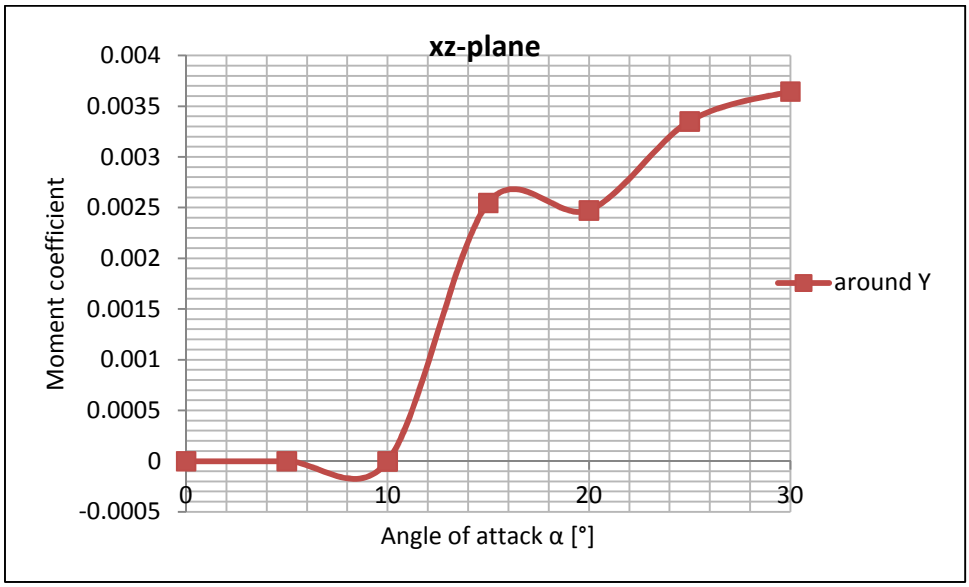

Figure 5.20: Moment coefficient acting on the ROV body in XZ-plane

In xz-plane, the moment coefficient around y-axis and the lift force are more important when increasing the angle of attack.

5.4.2. Streamlines

In figure 5.6, it was shown that the separated region at $\alpha = 0$ was symmetric behind the ROV body.

Figure 5.19 depicts the streamline patterns at the ROV section for different angles of attack ranging from 5° to 30° in xy-plane. It is observe that the separation region or the vortices behind the ROV body is reduced from $\alpha = 5°$ to $\alpha = 30°$. In the same xy-plane, it has been mentioned (*figure 5.17*) that the drag coefficient decreases in the same manner. Therefore, there is a linear dependence between the separated region and the drag pressure which is the main force acting on the ROV body in xy-plane. The larger separated region is, the larger the pressure drag is obtained.

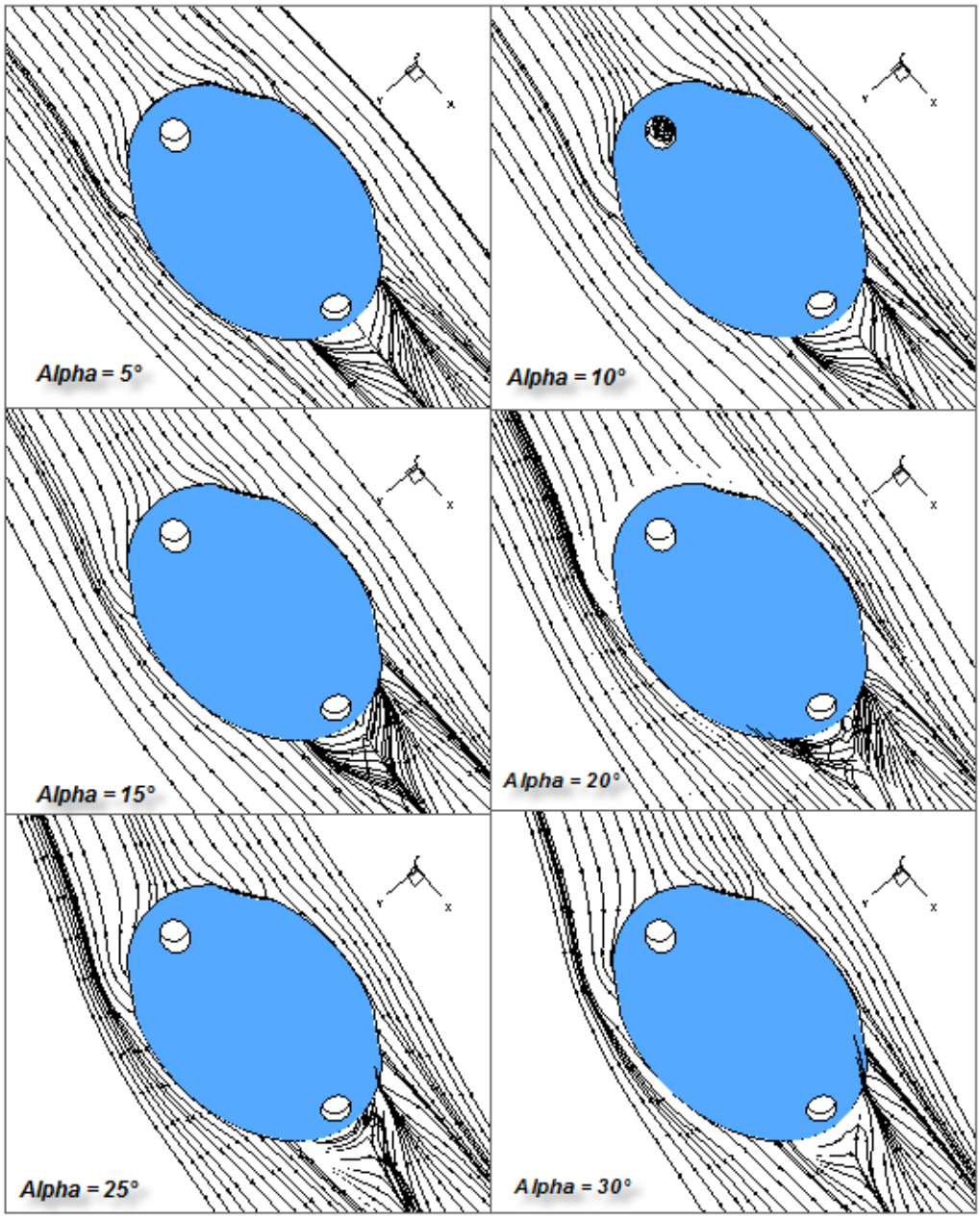

Figure 5.21: Streamline patterns at the ROV section for different angles of attack

CONCLUSION

The goal of the present work was to simulate turbulent flow around an ellipsoidal ROV body in order to investigate its propulsive performance. In order to do this, one investigation was done about existing ROV for modeling purpose and also Computational Fluid Dynamics simulation was performed at various velocities.

Turbulent flow around three fully submerged ellipsoids have been studied numerically using the commercial CFD code FLUENT. These three ellipsoids represent three configurations made in order to obtain more information about the elliptical ROV chosen according to the scope of the work and the existing ROV. These three configurations were “bare hull”, “ROV’s hull” and “ROV body”.

“Bare hull” was the elliptical ROV without cylindrical channels and propeller;

“ROV’s hull” was the elliptical ROV with cylindrical channels without propellers;

“ROV body” was the elliptical ROV with cylindrical channels and propellers.

These geometries have been designed with the CAD software Rhinoceros and the mesh generation was performed with the software GAMBIT.

Verification and Validation method from **ASME V&V 20 [17]** has been applied in order to determine the suitable turbulence model by calculating the discretization error.

Spalart-Allmaras turbulence model was finding as the best one to simulate turbulent flow around the ROV body with 0.14% of discretization error. At the same time was computing the validation uncertainty which was equal to 2%.

The numerical simulations have been performed around the ROV at five speeds of interest ranging from 1 m/s to 2 m/s. The resistance of the ROV based on the numerical was 13.53 N for the service speed of 3 knots. The corresponding effective power was 21 W. The numerical results show well agreement with experimental results.

Propellers were substituted by an active disk for which the pressure jump is defined as boundary conditions. The turbulent flow around the ROV body was characterized by flow separation inducing the creation of separated region behind the ROV. The effects of flow separation around the ROV body are felt in form of reduced velocity. The action of the propellers reduces the separation and the pressure gradient. Also, the separated region decreases in volume at high angle of attack.

The smaller separated region is, the smaller the ROV resistance is obtained leading to energy savings.

RECOMMENDATIONS FOR FURTHER WORK

When the propellers are considered during the simulation, the flow is already accelerated at the entrance of the channels. The entrance of the channels has been identified to be an accelerator of flow. For this reason, it would be interesting to redesign the entrance of the cylindrical channels and to perform unsteady computations.

ACKNOWLEDGEMENTS

This thesis was developed in the frame of the European Master Course in "Integrated Advanced Ship Design" named "EMSHIP" for "European Education in Advanced Ship Design", Ref.: 159652-1-2009-1-BE-ERA MUNDUS-EMMC.

REFERENCES

[1] **Roger L. Simpson** ''*Turbulent boundary layer separation,*'' Annual Reviews Fluid Mech., 21: 205-34, 1989.

[2] **Celik, I. B., et al**., "*Procedure for Estimation and Reporting of Uncertainty due to Discretization in CFD Applications*," ASME Journal of Fluids Engineering, Editorial, Vol. 130, No. 7, July 2008.

[3] **Munson; Young; Okiishi; Huebsch**, "*Fundamentals of fluid mechanics*"6th Edition, John Willey and Sons, 2010.

[4] **D. Obreja and L. Domnisoru** "*Theoretical and experimental investigation on the total resistance of an underwater ROV remotely operating vehicle*", Sustainable Maritime Transportation and Exploitation of Sea Resources – Rizzuto & Guedes Soares, 2012.

[5] **R. Gomes, A. Martins, A. Sousa, J. Sousa, S. Fraga, and F. Pereira** *"A new ROV design: issues on low drag and mechanical symmetry*". *Oceans 2005 – Europe*, Volume 2, pages 957 –962, 2005.

[6] **Costel Ungureanu and Adrian Lungu** ''*Unsteady 3D Turbulent Flow Separation around ROV body*'', *AIP Conference Proceedings* 1168, pages 685-689, 2009.

[7] **R. Sakthivel, S Vengaddesan and S K Bahattacharyya** ''*Application of non-linear κ-ε turbulence model in flow simulation over underwater axisymmetric hull at higher angle of attack*''. Journal of Naval Architecture and Marine Engineering, December, 2011.

[8] **Y. Eng W. Lau, E. Low, G. Seet, and C. Chin** "*Estimation of the Hydrodynamics Coefficients of an ROV using Free Decay Pendulum Motion*". *Engineering Letters* 16.3, 2008.

[9] **Imad Shukry Ali, Sahab Shehab Ahmed** ''*Modeling of Turbulent Separation Flow*'' World Academy of Science, Engineering and Technology, 2011.

[10] **J. L. Montagne** ‘‘the submersibles session’’. 20th ITTC Session Chair.

[11] **B. M. Sumer and J. fredsoe**. “*Hydrodynamics Around Cylindrical Structures.*” World Scientific Publishing Company, 2006. ISBN: 9812700390.

[12] **Roy, C.J.**, and Oberkampf et al., “A Complete framework for verification, Validation, and Uncertainty Quantification in scientific computing”, AAIA, 124, 2010.

[13] **G. Iaccarino, A. Ooi, P.A. Durbin, M. Behnia** ‘‘*Reynolds averaged simulation of unsteady separated flow*’’. International Journal of Heat and Fluid Flow, no. 24, pages 147–156, 2003.

[14] **L. Gentaz and Le Touze**, EMship lecture- CFD RANSE, 2012.

[15] ***Fluent Inc**. FLUENT User’s Guide version 6.3, 2006.

[16] ***ITTC**, 7.5-03.02.03, 2011.

[17] ***ASME V&V 20**, “*Standard for Verification and Validation in Computational Fluid Dynamics and Heat Transfer*”, American Society of Mechanical Engineers, 2009.

[18] **F. Stern, Robert V. Wilson, Hugh W**. **Coleman and Eric G. Paterson**, “*Verification and Validation of CFD simulations*”, Report no. 407, Iowa Institute of Hydraulic Research, 1999.

[19] **Roy, C. J.,** “*Review of the code and solution verification procedures for computational simulation*”, journal of Computational Physics, 205, 131-156, 2005.

[20] **L. Eça., M. Hoekstra** “*On the Influence of the Iterative Error in the Numerical Uncertainty of ship viscous flow calculations*”, 26 th Symposium on Naval Hydrodynamics, Rome, Italy, 17-22 September, 2006.

[21] **Volker Bertram**. “*Practical Ship Hydrodynamics*”. Butterworth Heineman, 2000.

[22**] J. P. Ghose, R. P. Gokarn** “*Basic Ship Propulsion*” Allied Publisher, 2004.

[23] **Roache, P. J**, “Quantification of uncertainty in computational fluid dynamics” Annual Reviews Fluid Mech., 29: 129-60, 1997.

APPENDIX A

A.1. Geometry

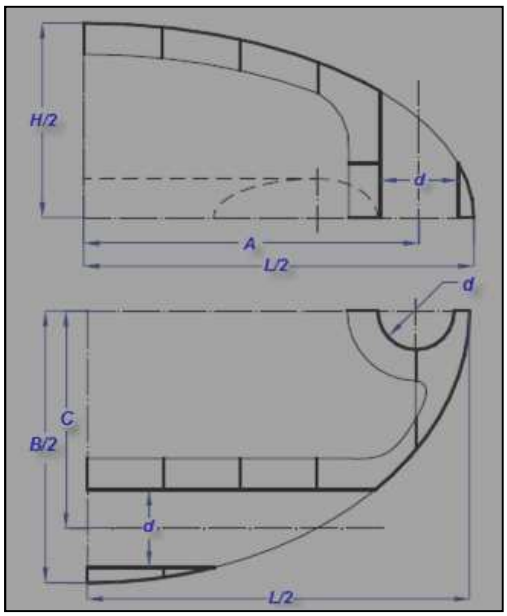

Figure A1: ROV's dimensions

Table A1: ROV's nomenclature

Characteristics	Symbol	Value
Length	*L*	500 [mm]
Width	*B*	350 [mm]
Height	*H*	250 [mm]
Horizontal spacing	*A*	215 [mm]
Vertical spacing	*C*	140 [mm]
Propellers diameter	*d*	50 [mm]

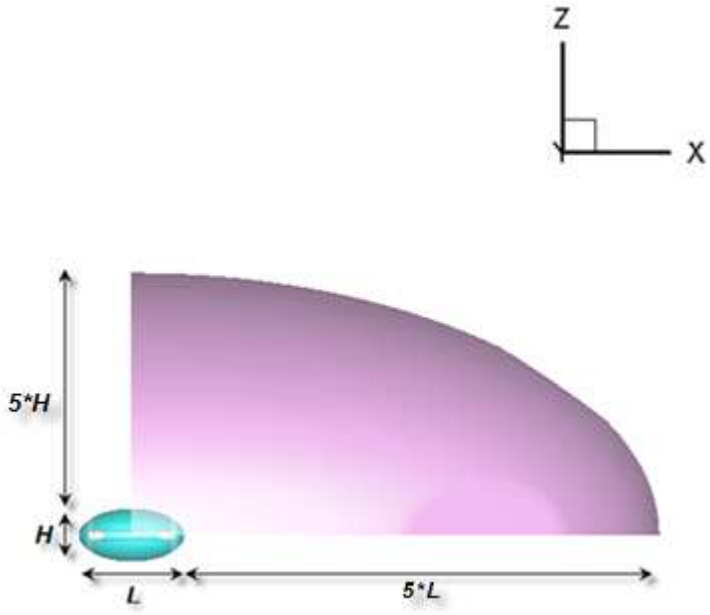

Figure A2: Dimensions of the computational domain, ROV body case

A.2: Meshes

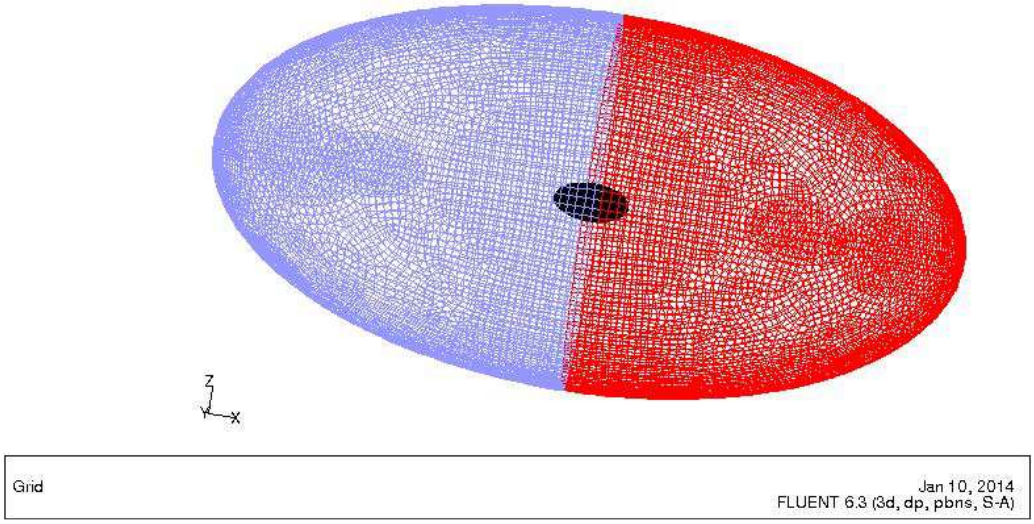

Figure A3: Grid on the entire computational domain

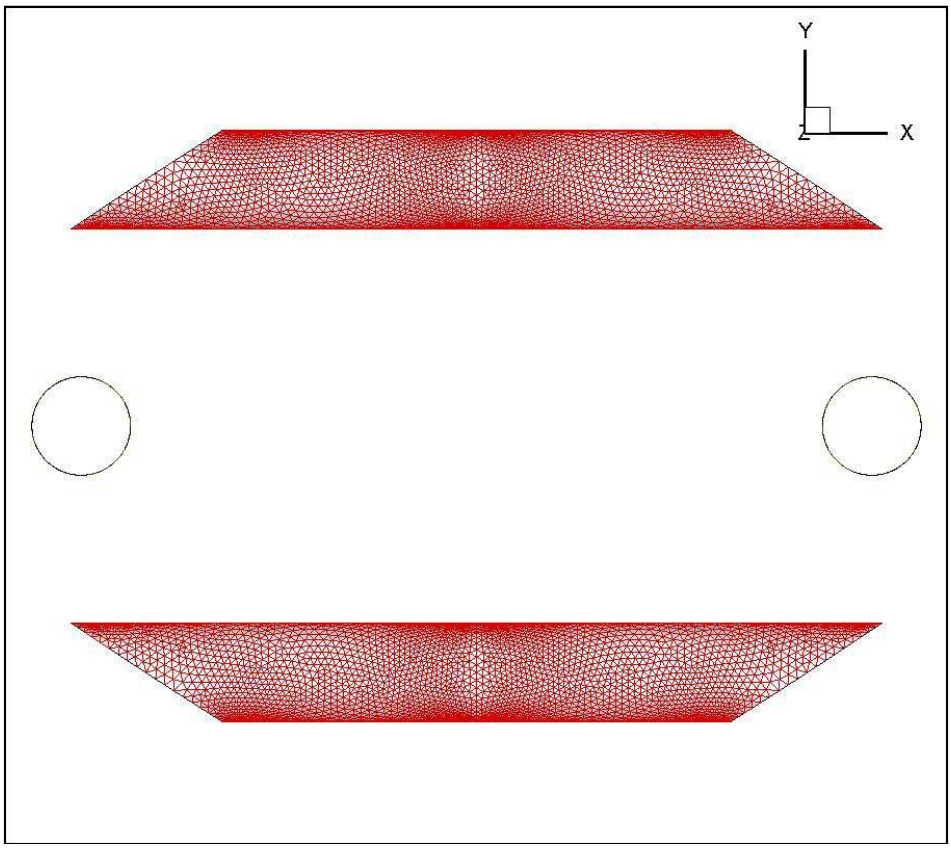

Figure A 4: Grid on horizontal channels

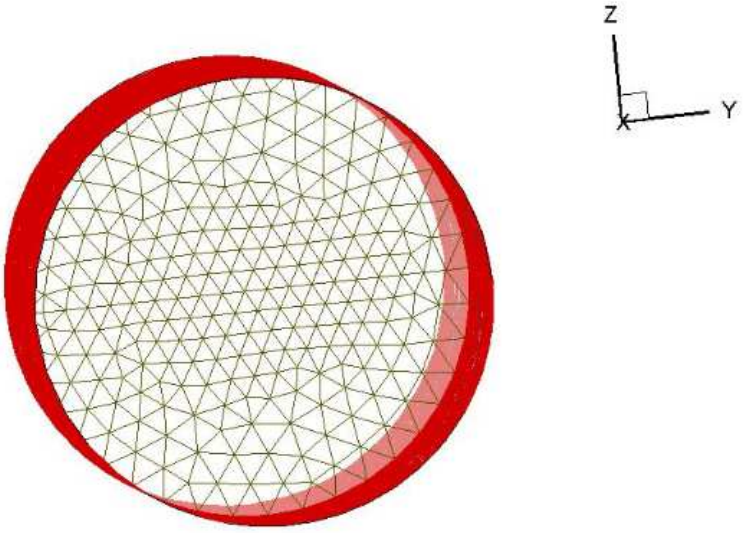

Figure A5: Grid on propeller plane

APPENDIX B

B.1: Reference values for service speed (All configurations)

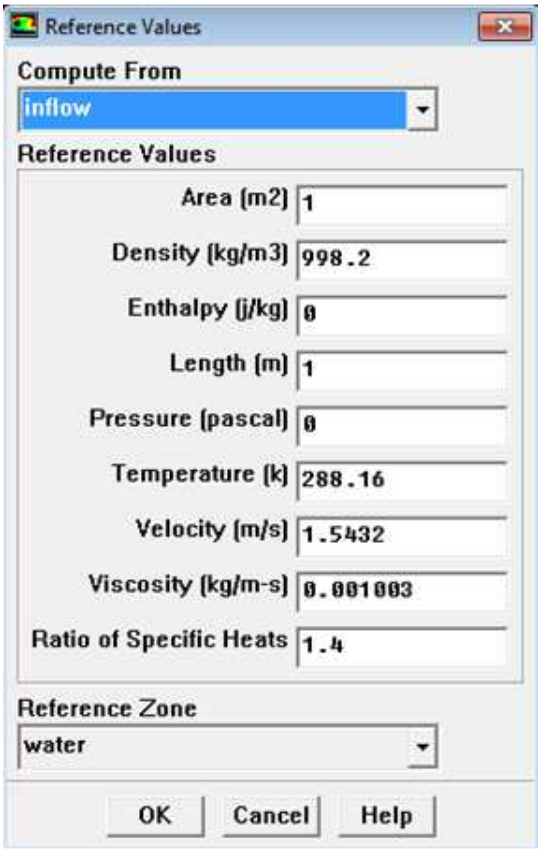

Figure B1: Reference values

B2: Residuals convergence

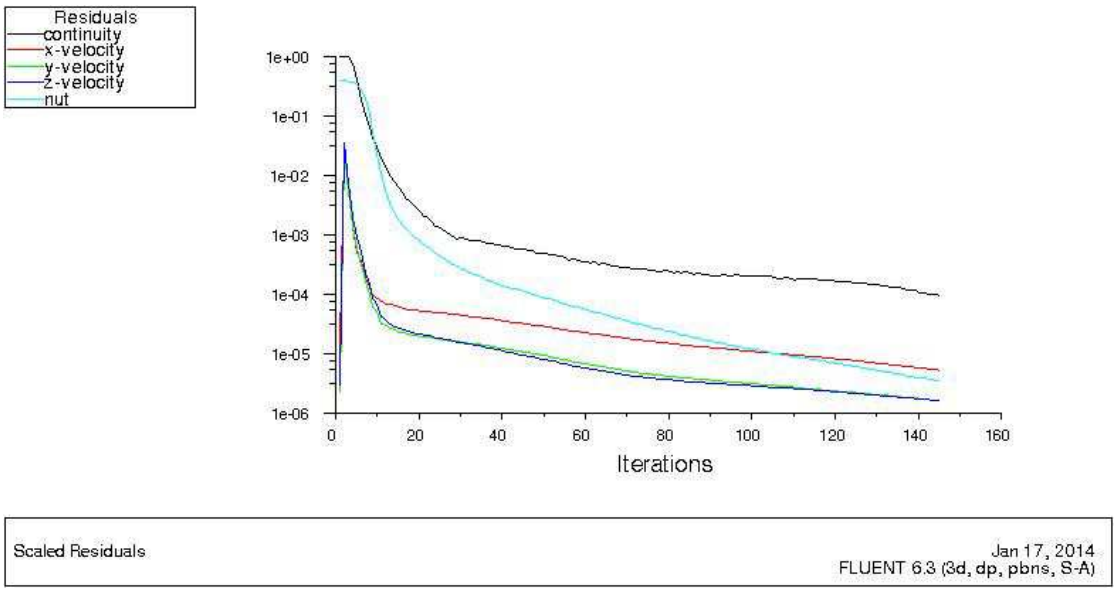

- Figure B2: Residuals convergence, bare hull case

B3: Streamlines

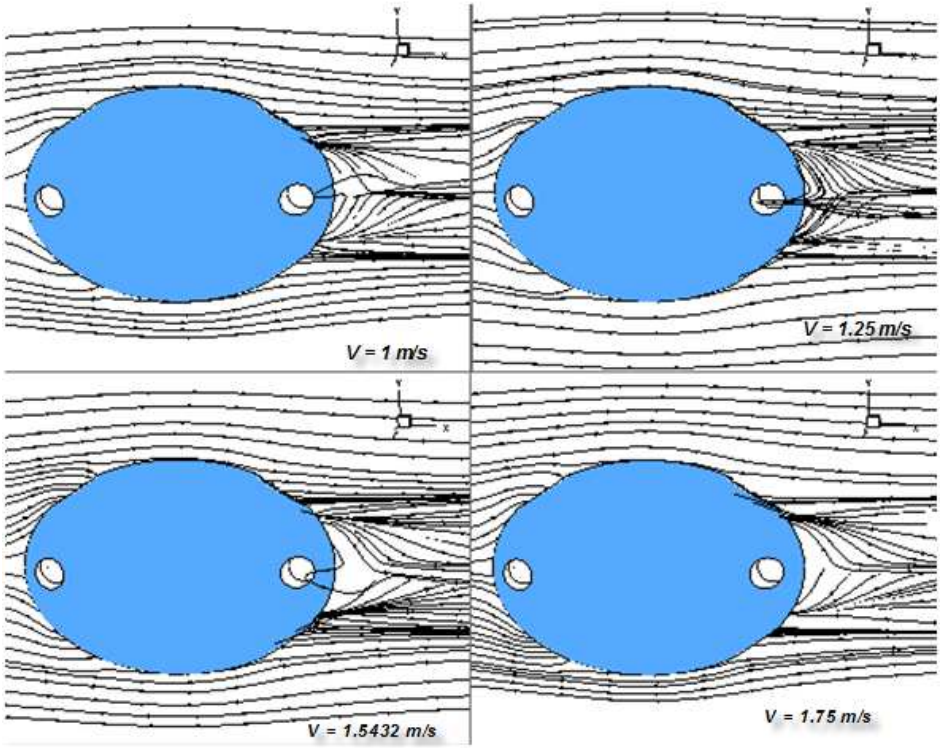

Figure B3: Streamline patterns at the ROV section for $\alpha = 0°$